

# **The Study of Flow and Non-flow Effects in Small Collision Systems**

**Pengqi Yin**

Department of Physics  
University of Colorado, Boulder

Advisor: Prof. James Nagle, Department of Physics

Prof. Michael Ritzwoller, Department of Physics

Mr. Donald Wilkerson, The Program for Writing and Rhetoric

Defense Date: March 20, 2017



# Abstract

Recent research at RHIC and the LHC suggests that a quark-gluon plasma (QGP) can also be formed in the collisions of small systems (e.g., d+Au, p+Pb). In large collision systems (e.g., Au+Au, Pb+Pb), the effect of flow in the QGP is large compared to other contributions, the so-called “non-flow” effects. However, in small collision systems, these non-flow effects are more dominant and must be better understood in order to extract the real flow signal from the data.

In this thesis, I present calculations of elliptic flow ( $v_2$ )— the second order momentum anisotropy coefficient— in d+Au, Au+Au, p+Pb, and Pb+Pb collisions at 20, 39, 62.5, 200 GeV and 5.02TeV from simulated data generated with the AMPT and the UrQMD models. The participant plane, the event plane, and the multi-particle cumulant methods are applied to analyze the simulated data.





## **Acknowledgements**

There are many people who have helped me with my work in the research group, and with the writing of this thesis. I would like to thank all of you.

Firstly I would like to thank my advisor, Professor Jamie Nagle. He provided me with this job and the opportunity to work with nice and smart people. Jamie has always been helpful and patient with me. I have learned a lot from him and I now find myself well prepared to pursue PhD studies.

I want to thank Javier Orjuela Koop and Sebastian Vazquez-Carson. They have helped me with my writing, and have helped me improve my English. I learned a lot from Javier since my first day on the job.

I would also like to thank Ron Belmont, Darren McGlinchey, Kurt Hill, and Theo Koblesky. You have all been supportive of my projects, and have provided an excellent atmosphere for physics in the lab.

Finally, I need to thank my family and friends. I appreciate my parents for supporting my studies abroad. I would like to thank Emma. She has always been there during the hardest times these years.



# Table of contents

<b>List of figures</b>	<b>ix</b>
<b>List of tables</b>	<b>xv</b>
<b>1 Introduction</b>	<b>1</b>
1.1 What is High Energy Nuclear Physics? . . . . .	1
1.2 How to Study the Quark Gluon Plasma? . . . . .	4
1.2.1 Relativistic Heavy-Ion Collider (RHIC) . . . . .	4
1.2.2 PHENIX detector . . . . .	6
1.3 Simulation Models of Heavy-ion Collision . . . . .	8
1.3.1 The SONIC and SuperSONIC Hydrodynamic Models . . . . .	8
1.3.2 AMPT Model . . . . .	8
1.3.3 UrQMD Model . . . . .	9
1.4 Thesis Goals . . . . .	10
<b>2 Overview of Heavy-Ion Collisions</b>	<b>11</b>
2.1 Event Characterization . . . . .	11
2.2 Anisotropic Flow . . . . .	13
2.3 Jet Quenching and Non-flow Effects . . . . .	15
<b>3 Analysis Methods</b>	<b>17</b>

3.1	Pseudorapidity . . . . .	17
3.2	Computing Azimuthal Anisotropy Relative to the Participant Plane of the Collision	18
3.3	Computing Azimuthal Anisotropy Relative to the Event Plane of the Collision	20
3.4	Multi-Particle Correlation (Cumulant) Method . . . . .	21
<b>4</b>	<b>Data and Results</b>	<b>25</b>
4.1	Measuring $dN_{ch}/d\eta$ in d+Au Events Generated with UrQMD . . . . .	25
4.2	Two-Particle Correlation Functions with Different $\eta$ Gaps in d+Au and p+p Collisions . . . . .	28
4.3	Comparing Different Analysis Methods in AMPT Simulations of d+Au Collisions	33
4.4	Reducing Non-flow Effects Through Multi-particle Correlation Methods . . . .	37
4.5	Centrality Dependence of Elliptic Flow in d+Au Collisions . . . . .	41
<b>5</b>	<b>Summary</b>	<b>43</b>
	<b>References</b>	<b>45</b>

# List of figures

1.1	Standard Model of Elementary Particles [1]. . . . .	2
1.2	Phase diagram of QCD in the temperature vs. baryon density plane. In the lower left panel, quarks and gluons are bound into hadrons. In the Quark-Gluon Plasma, quarks and gluons are no longer bound together. Colored circles indicate different quarks. . . . .	3
1.3	The time line shows the evolution of the Universe. . . . .	3
1.4	Relativistic Heavy-Ion Collider (RHIC). The red and green lines are the two beam lines. The PHENIX, STAR, PHOBOS, and BRAHMS experiments are located where the two rings intersect. Nuclei are initially accelerated in the booster and AGS (Alternating Gradient Synchrotron). Then the beam is inserted into the two beam lines and is accelerated to higher energies. [2] . . . . .	5
1.5	Evolution stages of a heavy ion collision. A) Pre-collision nuclei are relativistically flattened. B) The nuclei smash together and create a highly dense region. C) A QGP is created and the system expands at nearly speed of light. D) After 7 fm/c, the matter cools down enough for quarks and gluons to recombine to form hadrons. . . . .	6
1.6	The PHENIX detector configuration [3]. . . . .	7
1.7	Schematic representation of the PHENIX central arms, FVTX, and BBC detectors. [From J. D. Orjuela Koop] . . . . .	7

2.1	Illustration of a heavy-ion collision. The left picture depicts the state prior to the collision with an impact parameter, $b$ . The right picture shows the state after the collision. White particles are spectators, which are non-interacting nucleons. Other colored particles are participants, which are interacting nucleons [4]. . . . .	12
2.2	Charged particle distribution in the acceptance of the BBC-south detector, from AMPT simulations of d+Au events at 200 GeV. Different percentiles indicate centrality categories. . . . .	12
2.3	Schematic representation of the coordinate system used to describe particle collisions and the resulting particles. . . . .	13
2.4	Visualization to show the initial geometry of two large colliding nuclei with the same impact parameter. Red circles are participant nucleons, while yellow and orange circles are spectators. The left figure shows an example where the random distribution of nucleons creates a dominant elliptic flow. The right figure shows a similar event but now with a dominant triangular flow [5]. . . . .	14
2.5	Illustration of jet quenching [2]. . . . .	15
3.1	Pseudorapidity values for various angles. In high energy physics, we define the beam axis as $\theta = 0$ . Therefore, the positive beam axis has an infinitely large pseudorapidity. Particles with a trajectory along the positive beam axis have positive pseudorapidity, and those in the negative direction have negative pseudorapidity. Particles perpendicular to beam axis have zero pseudorapidity. $\eta \sim 0$ is called mid-rapidity, and $ \eta  \gg 1$ is called forward/backward rapidity. . . . .	18
3.2	The definition of the reaction plane and participant plane of a heavy-ion collision in the transverse plane. This shows the initial state nucleon or parton information taken from simulations after string melting and before parton scattering, which is only available in simulations. The vector in red is the impact parameter, $\vec{b}$ , the green circles are spectators, and the orange circles represent participant particles. . . . .	19

- 
- 3.3 The definition of the event plane of a heavy-ion collision along the transverse view, using final state hadron, similar to what is detected in actual experiments. The blue circles represent final state particles. . . . . 20
- 4.1 Pseudorapidity distribution of charged particles at four different collision energies. Minimum bias events ( $b < 20$  fm) were generated using the UrQMD model, version 3.4. Blue regions indicate the pseudorapidity acceptance of the north and south arms of the BBC detector ( $3.1 < |\eta| < 3.9$ ). The various simulated energies are labeled on the figure. . . . . 26
- 4.2 Pseudorapidity distribution of charged particles at four different collision energies. Central events ( $b < 2$  fm) were generated using the UrQMD model, version 3.4. Blue regions indicate the pseudorapidity acceptance of the north and south arms of the BBC detector ( $3.1 < |\eta| < 3.9$ ). The various simulated energies are labeled on the figure. . . . . 27
- 4.3 Pseudorapidity distribution of charged particles at four different collision energies. Central events ( $b < 2$  fm) were generated using the UrQMD model, version 3.4. Pink regions indicate the pseudorapidity acceptance of the north and south arms of the FVTX detector ( $1.0 < |\eta| < 3.0$ ). The various simulated energies are labeled on the figure. . . . . 27
- 4.4 Correlation functions as calculated from 3 million simulated d+Au central events at 200 GeV, including partonic and hadronic scattering stages. The red curve is a fit to the correlation function, whose first three Fourier harmonics are shown. The coefficients of the three harmonics are shown on upper left corner of each graph. . . . . 29
- 4.5 Same correlation functions as in the previous plot, for d+Au simulations where partonic and hadronic scattering have not been included. Same labels as the previous plot. . . . . 30

4.6	Correlation functions as calculated from 10 million central p+p collisions at 200 GeV, including partonic and hadronic scattering stages. Same labels as the previous plot. . . . .	30
4.7	Same correlation functions as in the previous plot, for p+p simulations where partonic and hadronic scattering have not been included. Same labels as the previous plot. . . . .	31
4.8	Correlation functions as calculated from 3 million central p+p collisions at 200 GeV, including partonic and hadronic scattering stages. Same labels as the previous plot. . . . .	31
4.9	Same correlation functions as in the previous plot, for d+Au simulations at 20 GeV, where partonic and hadronic scattering have not been included. Same labels as the previous plot. . . . .	32
4.10	Correlation functions as calculated from 10 million central p+p collisions at 20 GeV, including partonic and hadronic scattering stages. Same labels as the previous plot. . . . .	32
4.11	Same correlation functions as in the previous plot, for p+p simulations at 20 GeV, where partonic and hadronic scattering have not been included. Same labels as the previous plot. . . . .	33
4.12	The coordinates of partons (left) and initial state nucleons (right) from the same d+Au AMPT event. The eccentricity and second-order participant plane angle are listed on the upper-left corner. The red arrow indicates the direction of the participant plane. . . . .	34



- 4.13 (1) Top:  $v_2(p_T)$  in Au+Au collisions at 200 GeV from AMPT, measured using three different analysis methods: the two-particle cumulant method (pink cross), the event plane method relative to BBC-south region (green box), the parton participant plane method (solid circles), and the nucleon participant plane method (open circles). (2) Bottom: ratio of  $v_2$  from different methods to that from the parton participant plane. Same labels as in the top panel. . . . . 35
- 4.14 (1) Top:  $v_2(p_T)$  in d+Au collisions at 200 GeV from AMPT, measured using three different analysis methods. Labels are the same as shown in the previous plot. (2) Bottom: ratio of  $v_2$  from different methods to that from the parton participant plane. Same labels as in the top panel. . . . . 36
- 4.15 AMPT Simulation of p+Pb collisions at 5.02 TeV. (1) Top:  $v_2$  as a function of the number of charged particles in each event. The red curve is obtained using 2-particle cumulants (with an imposed  $\eta$  gap). The blue curve is from 4-particle cumulants. The solid black diamond curve is the result from the parton participant plane method. Finally, the open black diamond curve shows the results from Equation 3.19. (2) Bottom: ratio of the each set of results to those from the parton participant plane method. Same symbols as in top panel. 38
- 4.16 CMS results for  $v_2$  as a function of multiplicity in p+Pb collisions at 5.02 TeV. The red circles are the results from the 2-particle cumulant method. The open blue boxes are from the 4-particle cumulant method. The other symbols are described on the figure [6]. . . . . 39
- 4.17 Results from AMPT Pb+Pb events at 5.02 TeV. The labels are the same as in the figure showing the p+Pb results. . . . . 39
- 4.18 Results from AMPT Pb+Pb events at 5.02 TeV. (1) Top: fluctuations as a function of event multiplicity. The open triangles are the fluctuation of  $v_2$ . The solid triangles are the fluctuation of eccentricity ( $\epsilon_2$ ). (2) Bottom: ratio of the fluctuation of the eccentricity to the fluctuation of  $v_2$ . . . . . 40

---

4.19	Results from AMPT Au+Au events at 200 GeV. The red solid circle curve shows the result from the 2-particle cumulant method without imposing an $\eta$ gap. The other labels are the same as above. . . . .	40
4.20	Results from AMPT d+Au events at 200 GeV. The labels are the same as above.	41
4.21	Results from AMPT d+Au events at 200 GeV. Centralities are labeled on each graph. The red curve is $v_2$ from the event plane method, while the blue curve is $v_2$ from the parton participant plane method. . . . .	42

# List of tables

1.1	Nucleon-nucleon cross section for different collision energies. . . . .	9
-----	---	---



# Chapter 1

## Introduction

### 1.1 What is High Energy Nuclear Physics?

The Standard Model, developed during the latter half of the 20th century, is used to describe the elementary particles (Figure 1.1) and their interactions, which include the electromagnetic, weak, and strong interactions (gravity is not described by the Standard Model). Quantum Chromodynamics (QCD) is the theory that describes the strong nuclear force. The QCD potential between quarks can be written as:

$$V = -\frac{4}{3} \frac{\alpha_s}{r} + kr, \quad (1.1)$$

where  $\alpha_s$  is the coupling strength of the strong interaction,  $k$  is the string tension, and  $r$  is the distance between two quarks. When the distance is large ( $r \gg 1fm$ ), the second term will dominate the potential function. This describes the property of confinement, which requires that quarks and gluons be confined in hadrons, requiring an infinite amount of energy to be separated [4]. When the separation distance is small ( $r \ll 1fm$ ), the property of asymptotic freedom means the quarks will interact weakly.

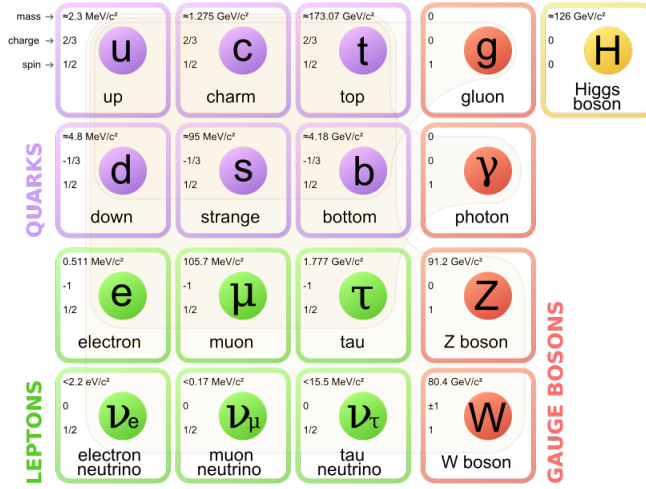


Fig. 1.1 Standard Model of Elementary Particles [1].

However, when nuclear matter is subjected to very high energy densities and high temperatures, the nuclear matter will undergo a phase transition to a deconfined state, called a Quark-Gluon Plasma (QGP) [7]. Quarks and gluons are then no longer bound in individual hadrons as shown in Figure 1.2. At low baryon density  $\mu_B$ , there is a smooth crossover from the hadronic to the QGP phase. At higher  $\mu_B$ , there will be a  $1^{st}$  order phase transition and a critical point (shown as a yellow dot in Figure 1.2), as predicted by lattice QCD calculations [8]. The QGP is the hottest form ( $10^{12}K$ ) of matter in the Universe, and it is predicted that the universe existed primarily in a QGP state just a few microseconds after the Big Bang, between the electroweak phase transition ( $t \sim 10^{-11}s$ ) and the strong phase transition ( $t \sim 10\mu s$ ). This is shown in Figure 1.3. During this QCD phase, the strong force held elementary particles together, confining quarks and gluons into hadrons (mesons and baryons), such as the proton.

In the present day, high energy physicists study QCD interactions over a wide range of energies (from several GeV to several TeV). This is primarily accomplished by colliding heavy ions. Over the past 20 years, the QGP has been the main research interest of the field of heavy-ion physics.

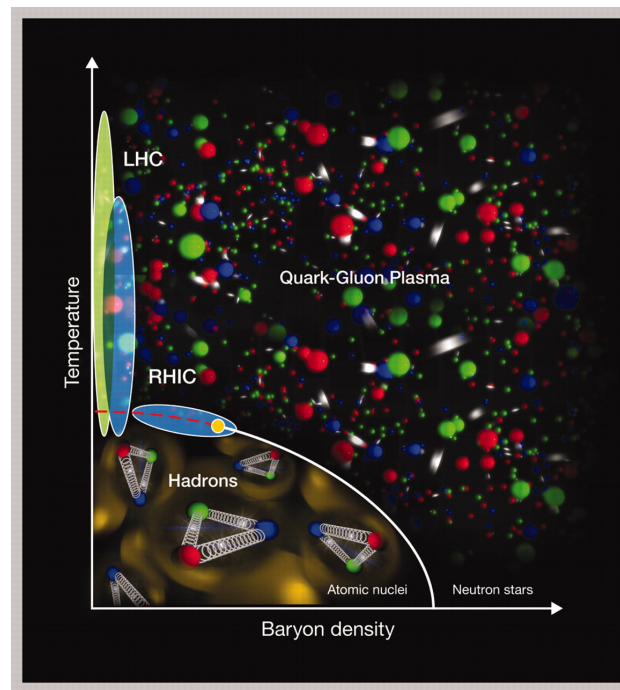


Fig. 1.2 Phase diagram of QCD in the temperature vs. baryon density plane. In the lower left panel, quarks and gluons are bound into hadrons. In the Quark-Gluon Plasma, quarks and gluons are no longer bound together. Colored circles indicate different quarks.

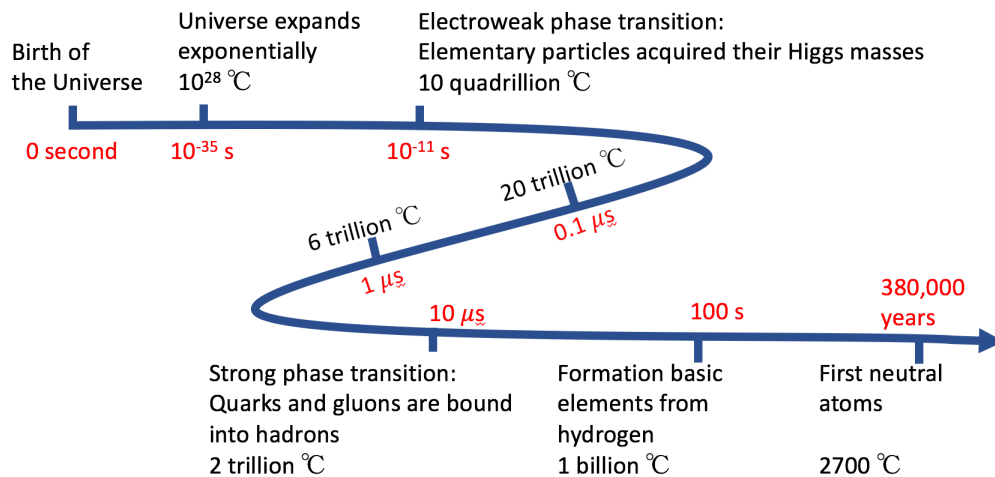


Fig. 1.3 The time line shows the evolution of the Universe.

## 1.2 How to Study the Quark Gluon Plasma?

Relativistic heavy-ion collisions provide a method to create and study the QGP, and the deconfining phase transition of QCD matter. Currently, there are two particle colliders that can do such experiments. One is the Large Hadron Collider (LHC), built by the European Organization for Nuclear Research (CERN), which has run collisions with a center-of-mass energy per nucleon from 1 TeV to 13 TeV. It has four main particle detector experiments: ALICE, ATLAS, CMS, and LHCb. The other accelerator capable of investigating the QGP is the Relativistic Heavy-Ion Collider (RHIC) in the U.S., which can achieve collision energies from 7.7 GeV to 200 GeV. PHENIX, STAR, PHOBOS, and BRAHMS have been the four major detectors at RHIC.

### 1.2.1 Relativistic Heavy-Ion Collider (RHIC)

The Relativistic Heavy-Ion Collider (RHIC) is funded by the U.S. Department of Energy and operated by Brookhaven National Lab with the aim of studying the QGP by colliding two beams of nuclei. It is the second-largest and second-highest-energy collider in the world and is the only collider capable of polarizing the proton's spin. There were two detectors running throughout 2016 at RHIC, PHENIX and STAR, as shown in Figure 1.4. PHOBOS and BRAHMS already completed their physics program and stopped taking data in 2005 and 2006, respectively. RHIC is composed of two beam lines (red and green circles in Figure 1.4), of 3.8 km in circumference. These two rings have 6 intersection points where nuclei can smash together. Different detectors are located at the different crossing points.

At relativistic energies, nuclei will be accelerated to more than 99% of the speed of light and then collided, thus achieving the extreme densities and temperatures required for QGP formation. For the past 15 years, RHIC has been recreating the QGP and studying its properties. Figure 1.5 shows an example of the evolution of a single large collision system (i.e. Au+Au) at RHIC. During the collisions, quarks and gluons can be freed for a short instant (the QGP formation time is about 0.7 fm/c) and the system continues to develop over its characteristic



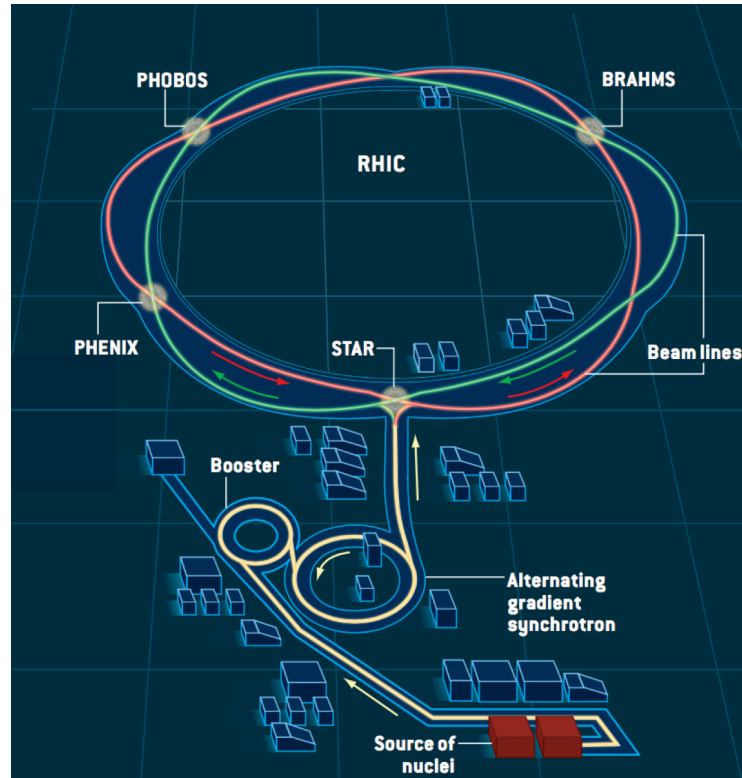


Fig. 1.4 Relativistic Heavy-Ion Collider (RHIC). The red and green lines are the two beam lines. The PHENIX, STAR, PHOBOS, and BRAHMS experiments are located where the two rings intersect. Nuclei are initially accelerated in the booster and AGS (Alternating Gradient Synchrotron). Then the beam is inserted into the two beam lines and is accelerated to higher energies. [2]

lifetime of about 7 fm/c. After hadronic scattering, thousands of particles are formed as the system cools down.

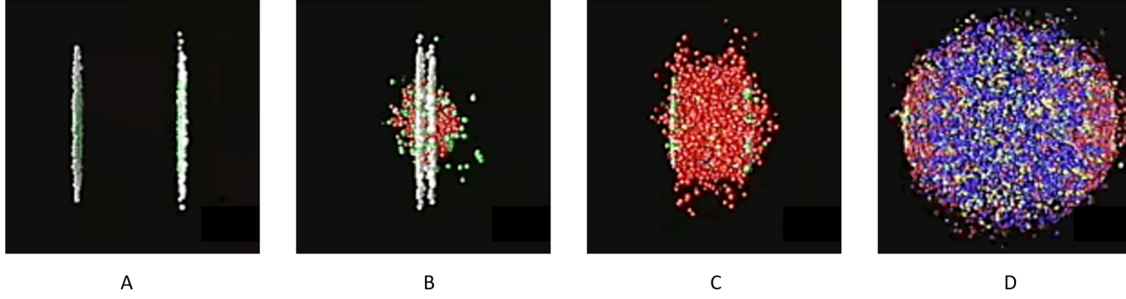


Fig. 1.5 Evolution stages of a heavy ion collision. A) Pre-collision nuclei are relativistically flattened. B) The nuclei smash together and create a highly dense region. C) A QGP is created and the system expands at nearly speed of light. D) After 7 fm/c, the matter cools down enough for quarks and gluons to recombine to form hadrons.

### 1.2.2 PHENIX detector

The PHENIX (Pioneering High Energy Nuclear Interaction eXperiment) was one of two, large detectors which operated at RHIC until 2016. It was designed for the investigation of heavy-ion collisions at high energies, which can help to study QCD matter and some other reaction processes. Two large central arm spectrometers measure and identify pions, kaons, and protons nearly perpendicularly to the beam axis. A set of muon arms are located to the south and north of the central spectrometers. See Figure 1.6.

Figure 1.7 is a zoomed-in view of the central arm spectrometers of PHENIX, which detect particles within a pseudorapidity range of  $-0.35 < \eta < 0.35$ . On either side of the central arms, there are two arms of the Forward Silicon Vertex Detector (FVTX), which cover the region  $1.0 < |\eta| < 3.0$ . There are also two Beam-Beam Counters ( $3.1 < |\eta| < 3.9$ ) located at very forward angles, providing information on the timing of collisions, as well as multiplicity measurements.

Since my projects are mostly based on simulations of heavy-ion collisions, and on comparing simulation results to real data, I will not describe the PHENIX detector in further detail.

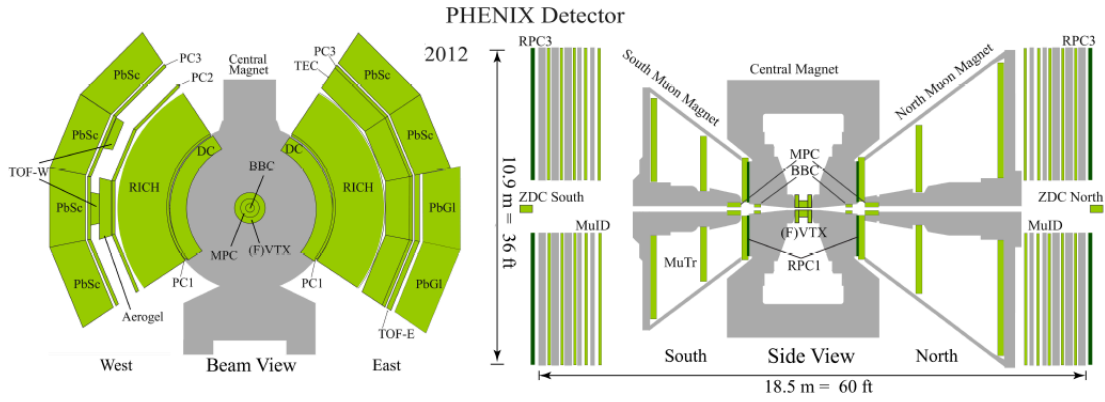


Fig. 1.6 The PHENIX detector configuration [3].

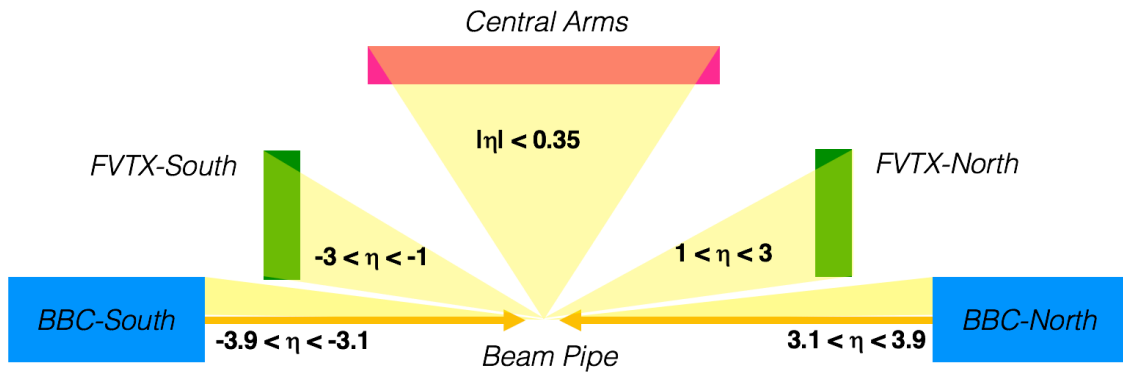


Fig. 1.7 Schematic representation of the PHENIX central arms, FVTX, and BBC detectors. [From J. D. Orjuela Koop]

## 1.3 Simulation Models of Heavy-ion Collision

In Figure 1.5, I described the stages of the evolution of a heavy-ion collision. Now I describe several theoretical models to simulate heavy-ion collision.

### 1.3.1 The SONIC and SuperSONIC Hydrodynamic Models

The “Super hybrid mOdel simulationN for relativistic heavy-Ion Collisions” (super-SONIC) [9] is a model which combines pre-equilibrium dynamics, hydrodynamic expansion, Cooper-Frye hadronization, and a late-stage hadronic cascade to describe all stages of the evolution of the medium. The initial geometry of the collision is translated into fluid cells [10] by hydrodynamics. Finally the late-stage hadronic cascade is modeled with the code B3D [11]. SuperSONIC successfully described particle distributions in d+Au collisions at RHIC, and the results are shown in Ref. [12].

### 1.3.2 AMPT Model

A-Multiphase-Transport model (AMPT) [13] is a transport model written for the study of heavy-ion collisions. AMPT uses Monte Carlo Glauber initial conditions generated via the HIJING model [14]. It is followed by a partonic interactions model, using Zhang’s Parton Cascade (ZPC), which contains two-body scattering with the screening mass obtained from the equation below for a given value of the interaction cross section,

$$\sigma_{part} = \frac{9\pi\alpha^2}{2\mu^2} \quad (1.2)$$

where  $\sigma_{part}$  is the cross section and  $\mu$  is the parton screening mass. In the final stage, AMPT includes a hadronic scattering phase to generate final state particles after spatial coalescence by pairing nearest neighbor partons.

The AMPT model provides a complete event record of initial state parton and nucleon spatial information, and records of the final state nucleons' 3-momentum, spatial coordinates, and mass at freeze-out. For each event, it also provides the impact parameter, the total number of participant nucleons in the projectile, and the total number of participant nucleons in the target. The record files from AMPT have been extensively used in my research project.

The default AMPT model only gives energy produced in hadronic strings, without any parton cascade, and it does not provide a good description of QGP flow. Therefore we use the a version of AMPT with a "string melting" mechanism, which converts all hadronic strings in the overlap region into parton strings [15].

By using the AMPT model, we can simulate different collision systems at different energies with different impact parameter ranges, as well as control the strength of the partonic and hadronic interactions. In this paper, we use AMPT version 2.26 with string melting turned on. Our group modified the AMPT source code to include the nuclear Hulthen wave function for the deuteron nucleus, in order to better describe its initial geometric configuration. By changing the default AMPT settings, we simulated a system with an initial interaction energy that depends on the nucleon-nucleon cross section ( $\sigma_{NN}$ ) [12] (See Table 1.1).

$\sqrt{s_{NN}}$ [GeV]	$\sigma_{NN}$ [mb]
20.0	32.5
39.0	34.3
62.4	36.0
200.0	42.3

Table 1.1 Nucleon-nucleon cross section for different collision energies.

### 1.3.3 UrQMD Model

The Ultrarelativistic Quantum Molecular Dynamics (UrQMD) model [16] is another transport model which contains the PYTHIA model, event-by-event fluctuations, and hadron resonance production.

UrQMD is widely used as a component of various transport models due to its accurate description of charged particle rapidity distributions. However, UrQMD does not include any interactions at the partonic level, and it thus provides a good contrast with models above.

## 1.4 Thesis Goals

In this thesis, I study a variety of observables to quantify the effects of flow and non-flow in d+Au, Au+Au, p+Pb, and Pb+Pb collisions at RHIC and LHC collision energies, using the AMPT v2.26 and UrQMD v3.4 event generators. I compare various methods to compute flow in different collision systems and at different collision energies. I also attempt to separate and understand the non-flow contribution to the measured flow signal with AMPT model simulations. I will present results that helped the PHENIX collaboration develop a set of data acquisition triggers for the d+Au beam energy scan in the spring of 2016. The experiment ran successfully and my calculations can be compared to actual measurements, which will be published soon by the PHENIX collaboration (including myself as co-author). My simulations reasonably reproduce the published flow measurements by the CMS experiment using different methods. Comparing these results to the true flow signal from the simulation have allowed us to understand how non-flow affects the results of different methods. I will show under which conditions these methods are least affected by non-flow.

This thesis is structured as follows. Section 2 introduces the concepts of flow and non-flow effects. Section 3 describes different methods that we used to analyze QGP flow. Section 4 contains a discussion of our results and a comparison with experimental measurements.

# Chapter 2

## Overview of Heavy-Ion Collisions

### 2.1 Event Characterization

In classical mechanics, the impact parameter,  $b$ , is defined as the perpendicular distance between the centers of two hard spheres, as indicated in Figure 2.1. Central collisions have  $b \approx 0$ , and peripheral collision have  $R < b < 2R$ , where  $R$  is the radius of the two colliding objects (assuming they are symmetric). In the collision of two large heavy ions (i.e. Au+Au), central events have the largest collision volume and highest density where the QGP features are expected to be detected.

In colliding-beam experiments at RHIC and the LHC, the nuclei are composed of nucleons which are made of tightly bound quarks. A central collision will typically produce the greatest number of particles. The impact parameter cannot be measured directly in experiments, so we use the charged particle multiplicity as a proxy of the collision centrality. Figure 2.2 shows the distribution of charged particles detected at forward rapidity in d+Au collisions at  $\sigma_{NN} = 200\text{GeV}$ , as simulated in the AMPT model. The 5% most central events are marked in red, and correspond to those with the largest number of particles. Correspondingly, the 60 – 100% centrality bin corresponds to the 40% of events with the lowest multiplicity.

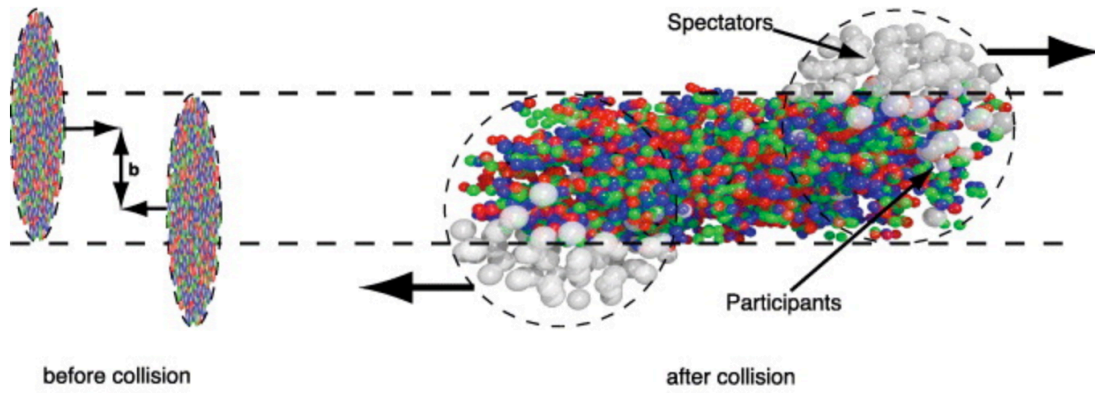


Fig. 2.1 Illustration of a heavy-ion collision. The left picture depicts the state prior to the collision with an impact parameter,  $b$ . The right picture shows the state after the collision. White particles are spectators, which are non-interacting nucleons. Other colored particles are participants, which are interacting nucleons [4].

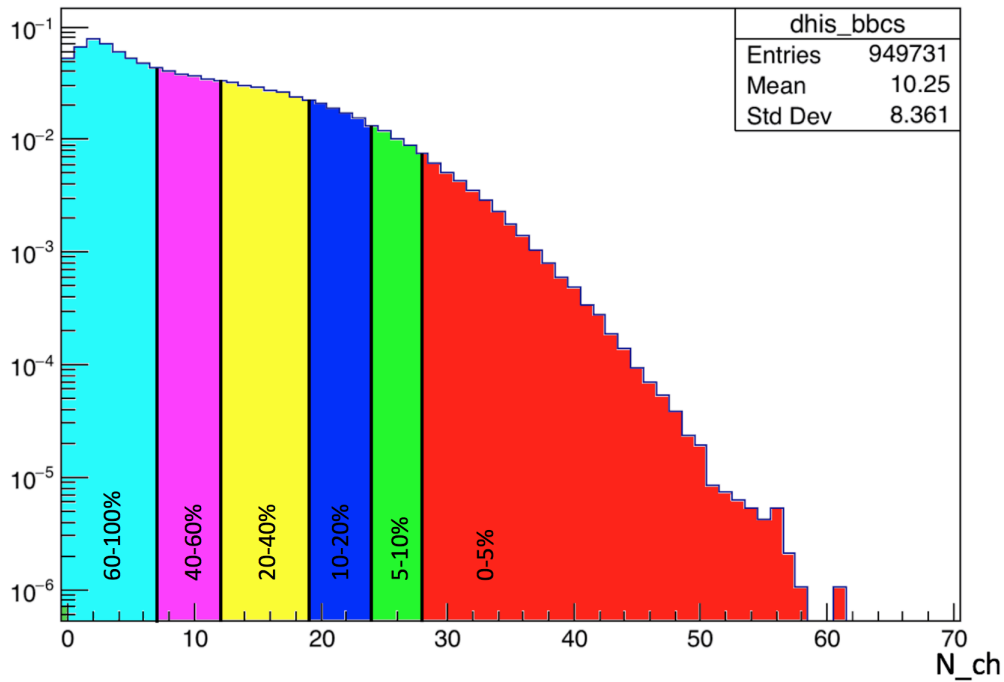


Fig. 2.2 Charged particle distribution in the acceptance of the BBC-south detector, from AMPT simulations of d+Au events at 200 GeV. Different percentiles indicate centrality categories.



The charged particle multiplicity is also related to the number of participating nucleons. Therefore, the centrality can also be calculated by inspecting participant nucleons within the framework of Glauber Monte Carlo calculations [17]. Accordingly, the Glauber Model is widely used in transport models for describing the collision geometry.

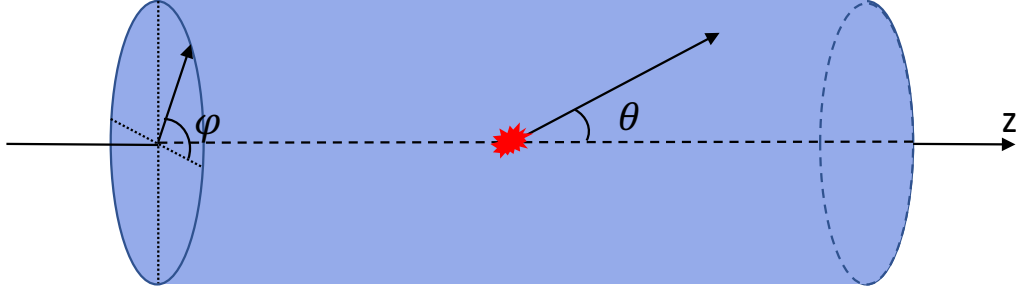


Fig. 2.3 Schematic representation of the coordinate system used to describe particle collisions and the resulting particles.

Figure 2.3 shows a general collision case where two beams of nuclei collide along the  $z$ -axis. The QGP will form at the red interaction point. Most produced particles will be detected by detectors around the cylinder. The particle's azimuthal angle is defined by the projection of momentum vector on the  $xy$ -plane.

## 2.2 Anisotropic Flow

During the collision, the system achieves a very large energy density and high temperature, which makes quarks and gluons undergo multiple interactions and form the QGP. The evolution leads to a collective expansion and cooling of particles before they eventually hadronize. This expansion is called flow. The magnitude of the flow is studied to describe the process of thermalization.

In heavy-ion physics, observations of anisotropic flow, an inhomogeneity in the  $\phi$  distribution of particles relative to the initial geometry, is the most direct evidence of flow. A convenient way to describe anisotropic flow is to use a Fourier expansion [4],

$$E \frac{d^3N}{d^3\mathbf{p}} = \frac{1}{2\pi} \frac{d^2N}{p_t dp_t dy} \left( 1 + 2 \sum_{n=1}^{\infty} v_n \cos[n(\varphi - \Psi_{RP})] \right) \quad (2.1)$$

where  $E$  is the energy of particle,  $p$  is the momentum vector,  $p_T$  is transverse momentum,  $\varphi$  is the azimuthal angle,  $v_n$  is the anisotropy coefficient, and  $\Psi_{RP}$  is reaction plane angle. The anisotropy coefficient depends on  $p_T$  and rapidity, as given by,

$$v_n = \langle \langle \cos[n(\varphi - \Psi_{RP})] \rangle \rangle \quad (2.2)$$

where the expectation value is calculated using all particles, summed over all events. In the decomposition,  $v_1$  is known as the directed flow coefficient,  $v_2$  is the elliptic flow coefficient,  $v_3$  is the triangular flow coefficient, and so on. When the shape of the region that is formed by the participant particles is elliptic (see the left panel of Figure 2.4), the anisotropic flow is dominated by elliptic flow, and  $v_2$  is much larger than the other coefficients.

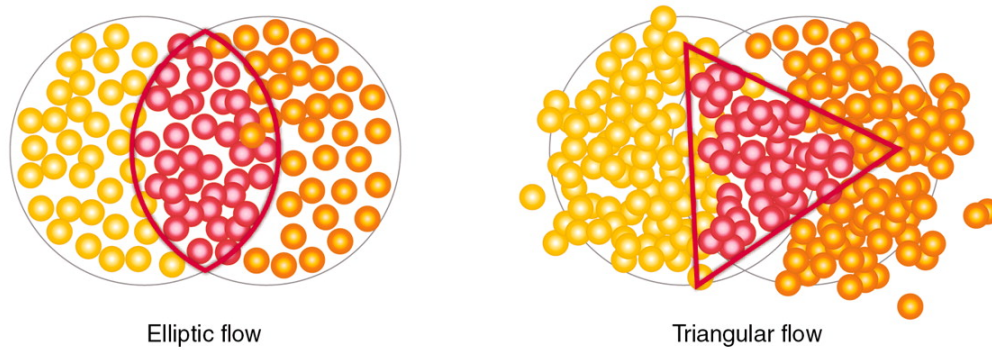


Fig. 2.4 Visualization to show the initial geometry of two large colliding nuclei with the same impact parameter. Red circles are participant nucleons, while yellow and orange circles are spectators. The left figure shows an example where the random distribution of nucleons creates a dominant elliptic flow. The right figure shows a similar event but now with a dominant triangular flow [5].

## 2.3 Jet Quenching and Non-flow Effects

As mentioned above, flow effects basically arise from initial geometry, QGP expansion, and hadronic interactions. However, the characteristic flow signal is not only generated by flow; there are also contributions that can mimic flow effects, referred to as non-flow. Momentum conservation is a good example of one of these so-called “non-flow” effects. Other non-flow effects include jet quenching, Coulomb interactions, and particle decays. These non-flow effects play a small role in large collision systems (e.g. Au+Au and Pb+Pb); however, they are more dominant in small collision systems (e.g. d+Au and p+Pb) and must be well understood in order to extract the real flow signal from the data. In this section, I will introduce jet quenching briefly.

Jet quenching is a phenomenon that commonly occurs in relativistic heavy-ion collisions. When partons (quarks or gluons) from two nuclei scatter off each other with a large momentum transfer, they then must traverse the medium. As they do so, the partons lose energy in the QGP and result in back-to-back jets of particles. Under extreme temperature conditions, these jets will interact strongly with the QGP and lose energy, exhibiting jet quenching as shown in Figure 2.5. The jet-quenching phenomenon has been observed in the study of the distributions of final-state momentum correlations at RHIC.

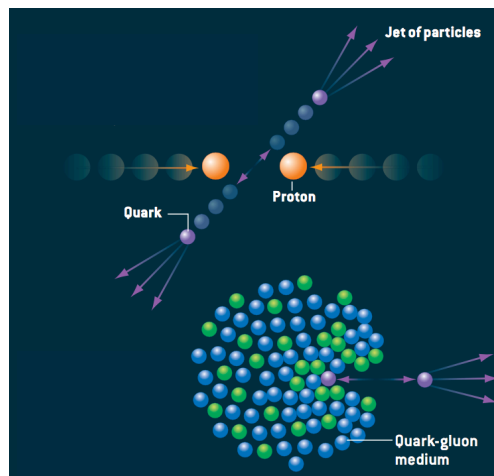


Fig. 2.5 Illustration of jet quenching [2].



# Chapter 3

## Analysis Methods

### 3.1 Pseudorapidity

Pseudorapidity is a widely used spatial coordinate that describes the angle between the direction of the particle and the beam axis. The pseudorapidity is defined as

$$\eta \equiv -\ln \left[ \tan \left( \frac{\theta}{2} \right) \right], \quad (3.1)$$

where  $\theta$  is the center-of-mass scattering angle between the particle's momentum and the positive beam axis, as shown in Figure 2.3. Some example pseudorapidity values are shown in Figure 3.1.

The reason we use pseudorapidity instead of the polar angle  $\theta$  is that differences in pseudorapidity are invariant under Lorentz boosts along the longitudinal direction. If we take a Lorentz transformation along the beam axis as an example, the tangent is simply the transverse displacement over the longitudinal displacement. Under the Lorentz transformation, the longitudinal displacement will be boosted by a factor of  $\gamma$ , as shown below:

$$\tan(\varphi) = \frac{x_T}{x_L} \quad \Rightarrow \quad \tan(\varphi') = \frac{x_T}{x_L/\gamma} = \gamma \tan(\varphi). \quad (3.2)$$

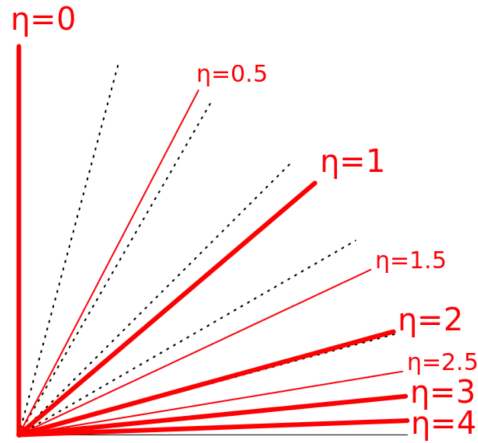


Fig. 3.1 Pseudorapidity values for various angles. In high energy physics, we define the beam axis as  $\theta = 0$ . Therefore, the positive beam axis has an infinitely large pseudorapidity. Particles with a trajectory along the positive beam axis have positive pseudorapidity, and those in the negative direction have negative pseudorapidity. Particles perpendicular to beam axis have zero pseudorapidity.  $\eta \sim 0$  is called mid-rapidity, and  $|\eta| \gg 1$  is called forward/backward rapidity.

If we plug this into the definition of pseudorapidity, we have

$$\eta = -\ln\left[\tan\left(\frac{\theta}{2}\right)\right] \Rightarrow \eta' = -\ln\left[\tan\left(\frac{\theta}{2}\right)\right] - \ln(\gamma). \quad (3.3)$$

As we can see, the  $\gamma$  term will cancel out when we take the difference in pseudorapidity of two particles.

## 3.2 Computing Azimuthal Anisotropy Relative to the Participant Plane of the Collision

The impact parameter,  $\vec{b}$ , and the beam direction,  $\vec{z}$ , define the plane in which the collision happens, also known as the reaction plane denoted as RP, see Figure 3.2. In simulations, we know the coordinates of all participant nucleons and partons in the collision. We can use this

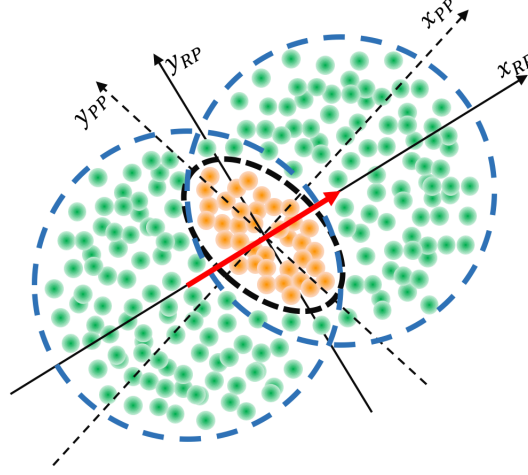


Fig. 3.2 The definition of the reaction plane and participant plane of a heavy-ion collision in the transverse plane. This shows the initial state nucleon or parton information taken from simulations after string melting and before parton scattering, which is only available in simulations. The vector in red is the impact parameter,  $\vec{b}$ , the green circles are spectators, and the orange circles represent participant particles.

information to calculate the reaction plane with the following equation:

$$\Psi_n = \frac{\arctan[\langle r^2 \sin(n\varphi) \rangle / \langle r^2 \cos(n\varphi) \rangle]}{n} + \frac{\pi}{n}, \quad (3.4)$$

where averages are taken over all the particles in each event. In the equation,  $r$  is the radial distance from the center of mass, and  $n$  is the order of the flow moment. The orientation of the participant zone,  $\Psi_n^{PP}$ , defines the participant plane orientation as shown in Figure 3.2.

Once  $\Psi_n^{PP}$  has been calculated, anisotropy coefficients can be defined as

$$v_n = \langle \langle \cos[n(\varphi_i - \Psi_n^{PP})] \rangle \rangle, \quad (3.5)$$

where the expectation value is taken over all particles in each event, and then averaged over all events [18].

The participant zone is defined by the initial geometry of the nucleons or the partons after string melting and before parton scattering. We cannot use this method in the analysis of real

data at RHIC or the LHC since we are unable to measure particle spatial information at the point where collisions happen. This method can only be implemented in simulations where we know the exact initial geometry. This method has the advantage of revealing the true flow contributions.

### 3.3 Computing Azimuthal Anisotropy Relative to the Event Plane of the Collision

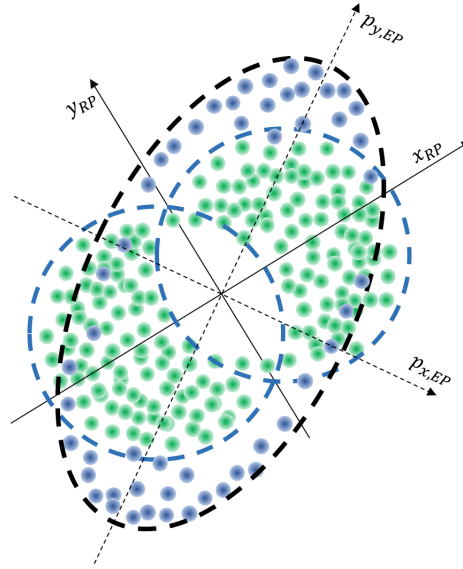


Fig. 3.3 The definition of the event plane of a heavy-ion collision along the transverse view, using final state hadron, similar to what is detected in actual experiments. The blue circles represent final state particles.

In the experiment, we cannot access the spatial coordinates of the participants. Therefore, the only quantities that are available are the final state particle momenta as measured by our detectors. We can use these particles to estimate  $\Psi_n$ . The event plane coordinate system is defined by the particles' final-state information. The flow vector  $\vec{Q}$  is expressed as

$$\vec{Q} = \{Q_x, Q_y\} = \left\{ \sum \cos(n\phi_i), \sum \sin(n\phi_i) \right\}, \quad (3.6)$$



where  $\varphi_i$  is the azimuthal angle of each the momentum vector of each particles. The flow vector is the sum of particles selected within some specific pseudorapidity range. The orientation of the flow vector defines the event plane  $Psi_n$  as shown in Figure 3.3,

$$\Psi_n^A = \frac{\arctan[\langle Q_y \rangle / \langle Q_x \rangle]}{n} \quad (3.7)$$

where  $Q_y$  and  $Q_x$  are averaged over all particles in each event [18]. Given the limited number of final state particles, we must apply a correction to the anisotropy coefficients,  $v_n$ , to account for the resolution of the measured event plane. This resolution is estimated from the correlation between different sub-events, where a sub-event is a subset of the final particles in a given acceptance. If we have two sub-events with the same resolution, we can calculate the resolution as follows:

$$Res(\Psi) = \langle \cos[n(\Psi_n^A - \Psi_n^B)] \rangle = \sqrt{\langle \cos[n(\Psi_n^A - \Psi_n^B)] \rangle} \quad (3.8)$$

where  $n$  is the harmonic number. However, if we use particles from different acceptances, these sub-events are not equal; therefore, The resolutions are different from each other. We need at least three sub-events to apply the three-subevent method to calculate the resolutions:

$$Res(\Psi_n^A) = \sqrt{\frac{\langle \cos[n(\Psi_n^A - \Psi_n^B)] \rangle \langle \cos[n(\Psi_n^A - \Psi_n^C)] \rangle}{\langle \cos[n(\Psi_n^B - \Psi_n^C)] \rangle}}, \quad (3.9)$$

where the expectation value is taken over all particles in each event, and  $\varphi_i$  is the azimuthal angle of each particle [19]. The event plane method is sensitive to both flow and non-flow contributions.

### 3.4 Multi-Particle Correlation (Cumulant) Method

Measurements in heavy-ion collision comprise both correlations arising from flow (i.e. related to initial geometry and medium expansion), and non-flow (i.e. from elementary processes such

as momentum conservation and jet quenching). Multi-particle correlation (cumulant) methods are a way to remove non-flow contributions and improve measurements of anisotropic flow [20]. The methods involves correlations among different numbers of particles, in particular 2-particle, 4-particle and 6-particle correlations. The simplest case involves 2 particles, and is given by,

$$v_2^2\{2\} = \langle 2 \rangle = \langle e^{ie(\varphi_1 - \varphi_2)} \rangle = \langle \cos[2(\varphi_1 - \varphi_2)] \rangle = \langle v_2 \rangle^2 + \sigma^2 + \delta^2 \quad (3.10)$$

where  $\langle v_2 \rangle^2$  is the flow contribution and  $\sigma^2$  comes from fluctuations, and  $\delta$  represents non-flow effects [20]. The 4-particle correlation can be written as

$$v_2^2\{4\} = \langle 4 \rangle = \langle e^{ie(\varphi_1 + \varphi_2 - \varphi_3 - \varphi_4)} \rangle = (2\langle v_2^2 \rangle^2 - \langle v_2^4 \rangle)^{1/2} \approx \langle v_2 \rangle^2 - \sigma^2 - \delta^2 \quad (3.11)$$

The 6-particle correlation is

$$v_2^2\{6\} = \langle 6 \rangle = \langle e^{ie(\varphi_1 + \varphi_2 + \varphi_3 - \varphi_4 - \varphi_5 - \varphi_6)} \rangle \approx \langle v_2 \rangle^2 - \sigma^2 - \delta^2 \quad (3.12)$$

In practice, computing these correlations involves looping over all particles forming all possible combinations of 2, 4 and 6 particles. It needs  $O(n^2)$  time to generate 2-particle correlations, which is not a big deal since we only have approximately 100 particles per event produced in d+Au at 200 GeV. However, it will take  $O(n^4)$  and  $O(n^6)$  time to generate 4-particle and 6-particle correlations, which makes the calculation infeasible for events with high final state multiplicities. Therefore, we use the cumulant formalism [20], which involves some approximations, to get correlation functions and avoid the problem of combinatorics. The second harmonic cumulant is the average of 2-particle correlations. By separating diagonal and non-diagonal terms of  $|Q_n|^2$ , we simply obtain,

$$v_n\{2\} = \sqrt{c_n\{2\}} = \sqrt{\langle \langle 2 \rangle \rangle} \quad (3.13)$$

where,

$$\langle 2 \rangle = \frac{|Q_n|^2 - M}{M(M-1)} \quad (3.14)$$

where M is the multiplicity of each event, that is the number of charged particles in each event.

And 4-particle cumulant is given by

$$v_n\{4\} = \sqrt[4]{-c_n\{4\}} = \sqrt[4]{-\langle\langle 4 \rangle\rangle + 2 \cdot \langle\langle 2 \rangle\rangle^2}, \quad (3.15)$$

where

$$\langle 4 \rangle = \frac{|Q_n|^4 + |Q_{2n}|^2 - 2\Re[Q_{2n}Q_n^*Q_n^*] - 4(M-2)|Q_n|^2 + 2M(M-3)}{M(M-1)(M-2)(M-3)}, \quad (3.16)$$

where  $Q_n$  and  $Q_{2n}$  are flow vectors summed over all selected particles in each event.

The 6-particle cumulant is

$$v_n\{6\} = \sqrt[6]{\frac{1}{4}c_n\{6\}} = \sqrt[6]{\frac{1}{4}(\langle\langle 6 \rangle\rangle - 9 \cdot \langle\langle 2 \rangle\rangle\langle\langle 4 \rangle\rangle + 12 \cdot \langle\langle 2 \rangle\rangle^3)}, \quad (3.17)$$

where

$$\begin{aligned} \langle 6 \rangle = & \frac{|Q_n|^6 + 9 \cdot |Q_{2n}|^2 |Q_n|^2 - 6 \cdot \Re[Q_{2n}Q_n^*Q_n^*Q_n^*]}{M(M-1)(M-2)(M-3)(M-4)(M-5)} \\ & + \frac{4 \cdot \Re[Q_{3n}Q_n^*Q_n^*Q_n^*] - 12\Re[Q_{3n}Q_{2n}^*Q_n^*]}{M(M-1)(M-2)(M-3)(M-4)(M-5)} \\ & + \frac{18(M-4) \cdot \Re[Q_{2n}Q_n^*Q_n^*] + 4 \cdot |Q_{3n}|^2}{M(M-1)(M-2)(M-3)(M-4)(M-5)} \\ & - \frac{9|Q_n|^4 + |Q_{2n}|^2}{M(M-1)(M-2)(M-3)(M-5)} \\ & + \frac{18|Q_n|^2}{M(M-1)(M-3)(M-4)} \\ & - \frac{6}{(M-1)(M-3)(M-5)}. \end{aligned} \quad (3.18)$$

In large collision systems like Au+Au and Pb+Pb, the non-flow contributions and fluctuations will on average be negligible due to high multiplicity. However, in small collision system

like p+Au, p+Pb, d+Au, and  $^3\text{He}+\text{Au}$ , non-flow effects and fluctuations are more dominant and must be accounted for in order to draw accurate conclusions. With Equations 3.11 and 3.12, the pure flow effect can be approximately eliminated by using two different multi-particle cumulant methods as shown below:

$$\langle v_2 \rangle^2 = \frac{v_2^2\{2\} + v_2^2\{4\}}{2}, \quad (3.19)$$

and the fluctuations can be calculated as

$$\langle \sigma_2 \rangle^2 = \frac{v_2^2\{2\} - v_2^2\{4\}}{2}. \quad (3.20)$$

# Chapter 4

## Data and Results

In this chapter we describe the calculation of  $v_2$  in small collision systems, for various cases where we vary the event generator, the collision system, the analysis method, and the acceptance requirement imposed on events. Additional calculations are also presented.

### 4.1 Measuring $dN_{ch}/d\eta$ in d+Au Events Generated with UrQMD

In order to study small collision systems, we need to conduct actual experiments at the LHC or RHIC. This simulation study was carried out to support the PHENIX proposal of running d+Au collisions at RHIC in 2016. Unlike AMPT, UrQMD is an event generator which describes the Fermi motion of spectator nucleons. Because of this, UrQMD gives a reasonable description of the charged particle rapidity distribution (in particular for collision spectators) over a range of energies from 20 GeV to 200 GeV.

In this study, we used the UrQMD model, version 3.4, to simulate d+Au collisions at four different collision energies. A sample of minimum bias events with impact parameter  $b < 20$ , containing both central and peripheral events, was generated at each energy. As shown in Figure 4.1, the spectators can be clearly identified as peaks on both ends of the  $dN_{ch}/d\eta$

distribution within  $-10 < \eta < 10$ . In contrast, the same distribution generated with the AMPT model did not exhibit the spectator peaks, but instead decreased smoothly on either end.

As expected, for energies greater than 10 GeV, no spectators can fire the BBC detectors on both the south and north sides (See Figure 4.1). In Figure 4.2, we see that at low collision energies, very few particles are emitted in the deuteron-going direction that would hit the BBC-North detector, even when selecting central events exclusively ( $b < 2$  fm). However, if we look at the pseudorapidity acceptance of the FVTX detector (as shown in Figure 4.3), we find more particles there to fire the detectors. Therefore, the FVTX could function as a good trigger detector. Therefore, this study provided evidence that the FVTX detector could be used to develop a trigger for d+Au collisions event at low energies.

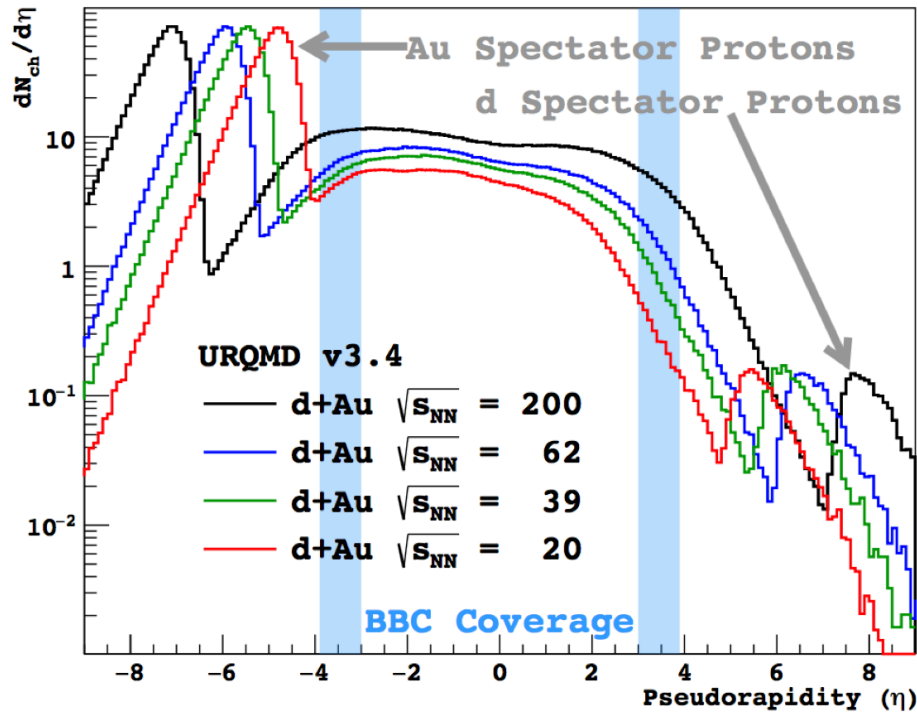


Fig. 4.1 Pseudorapidity distribution of charged particles at four different collision energies. Minimum bias events ( $b < 20$  fm) were generated using the UrQMD model, version 3.4. Blue regions indicate the pseudorapidity acceptance of the north and south arms of the BBC detector ( $3.1 < |\eta| < 3.9$ ). The various simulated energies are labeled on the figure.

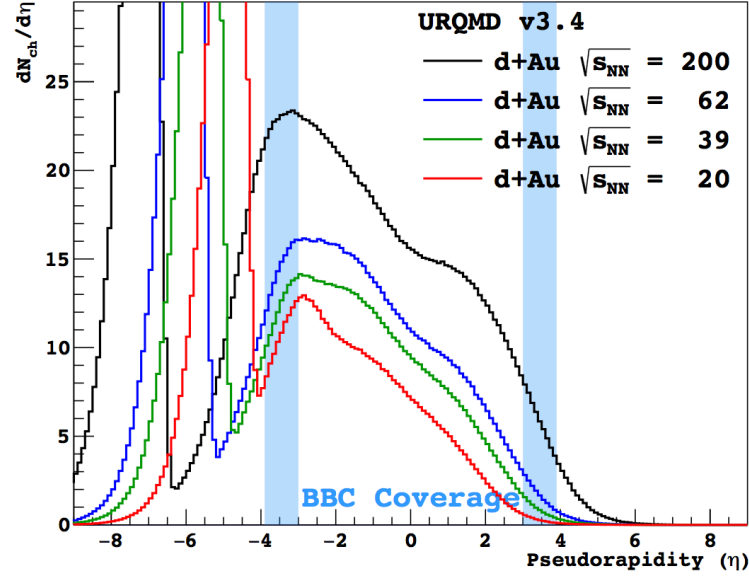


Fig. 4.2 Pseudorapidity distribution of charged particles at four different collision energies. Central events ( $b < 2$  fm) were generated using the UrQMD model, version 3.4. Blue regions indicate the pseudorapidity acceptance of the north and south arms of the BBC detector ( $3.1 < |\eta| < 3.9$ ). The various simulated energies are labeled on the figure.

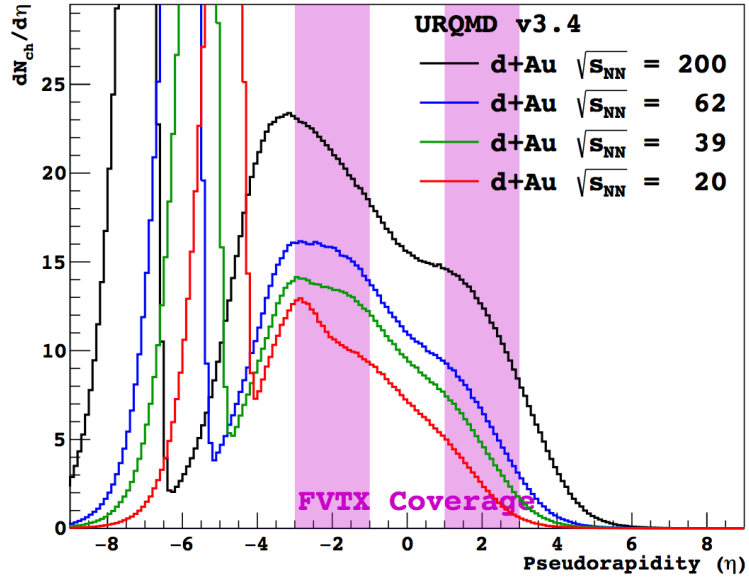


Fig. 4.3 Pseudorapidity distribution of charged particles at four different collision energies. Central events ( $b < 2$  fm) were generated using the UrQMD model, version 3.4. Pink regions indicate the pseudorapidity acceptance of the north and south arms of the FVTX detector ( $1.0 < |\eta| < 3.0$ ). The various simulated energies are labeled on the figure.

## 4.2 Two-Particle Correlation Functions with Different $\eta$ Gaps in d+Au and p+p Collisions

A correlation function is a function that describes the statistical correlation among variables. In this section, we present the correlations constructed with particle pairs, by comparing their azimuthal angles.

The main idea of this project is to study how imposing different  $\eta$  gaps between the two particles impacts the two-particle correlation functions. We used AMPT version 2.26 to simulate central d+Au and p+p collisions ( $b < 2$  fm) at  $\sqrt{s_{NN}} = 200$  and 20 GeV. We then carried out the simulations again, turning off the hadronic and partonic scattering stages, effectively removing all flow effects, leaving only non-flow contributions. Two-particle correlations were then calculated by selecting random pairs of particles at mid-rapidity ( $|\eta| < 1$ ) and taking the difference of their azimuthal angles (adjusted to the range  $-\frac{\pi}{2} < \Delta\phi < \frac{3\pi}{2}$ ).

Figure 4.4 shows the correlation functions and their Fourier decomposition for d+Au collisions at 200 GeV, with four different  $\eta$  gaps imposed. The second harmonic for the case of the smallest  $\eta$  gap is significantly less dominant than in the case of the largest  $\eta$  gap. There is a clear peak around  $\Delta\phi \approx 0$  which is dominated by flow effects. The absence of a peak when a small  $\eta$  gap is imposed can be explained from non-flow effects. As simulated here, this non-flow effect can be reduced by imposing a large  $\eta$  gap of around  $|\Delta\eta| \sim 2$ .

Figure 4.5 shows two-particle correlations when partonic and hadronic scattering are not included in the simulation. The shape of the function clearly indicates non-flow effects, primarily momentum conservation and also possibly elementary processes. As before, imposing a large  $\eta$  gap also removes contributions from non-flow effects. In p+p collisions, as shown in Figure 4.6 and 4.7, the directed flow should be the dominant source of the flow signal. As expected, we observed a large first order harmonic in the correlation function.



The results for d+Au and p+p collisions at 20 GeV are shown in Figure 4.8 ~ Figure 4.11. The correlation functions shown in Figure 4.8 with a large  $\eta$  gap still provide evidence of elliptic flow, though its magnitude is not as significant as in the case of collisions at 200 GeV.

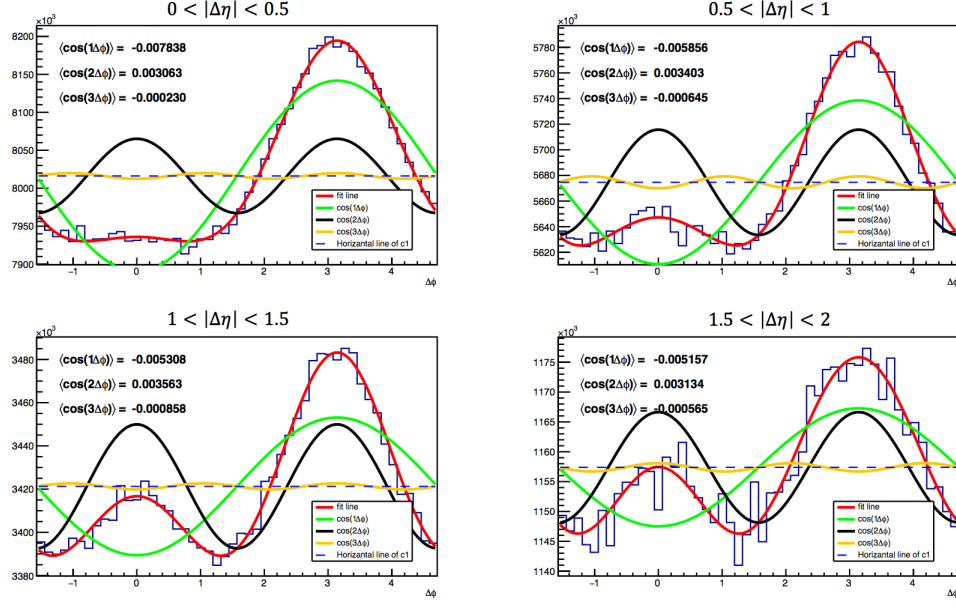


Fig. 4.4 Correlation functions as calculated from 3 million simulated d+Au central events at 200 GeV, including partonic and hadronic scattering stages. The red curve is a fit to the correlation function, whose first three Fourier harmonics are shown. The coefficients of the three harmonics are shown on upper left corner of each graph.

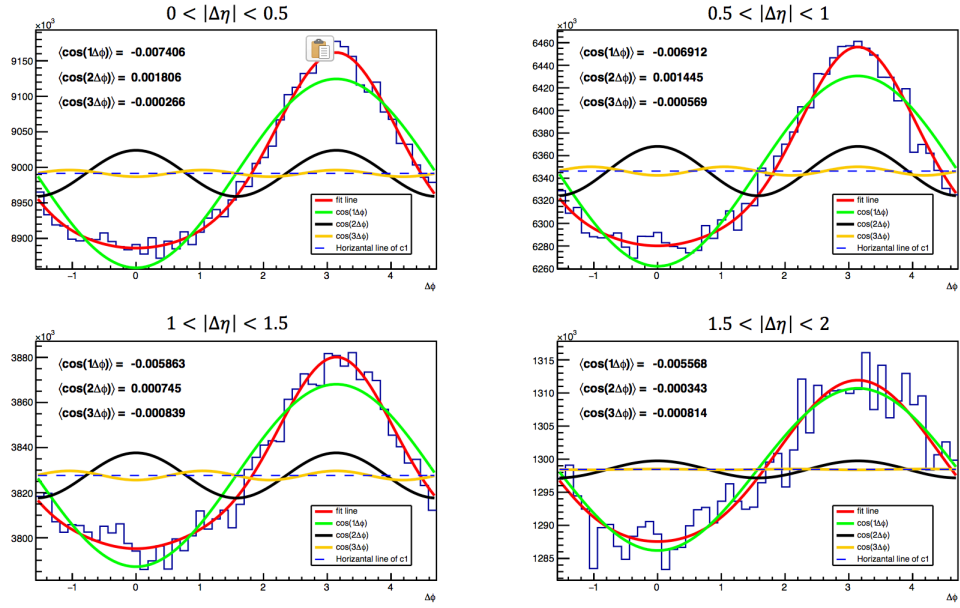


Fig. 4.5 Same correlation functions as in the previous plot, for d+Au simulations where partonic and hadronic scattering have not been included. Same labels as the previous plot.

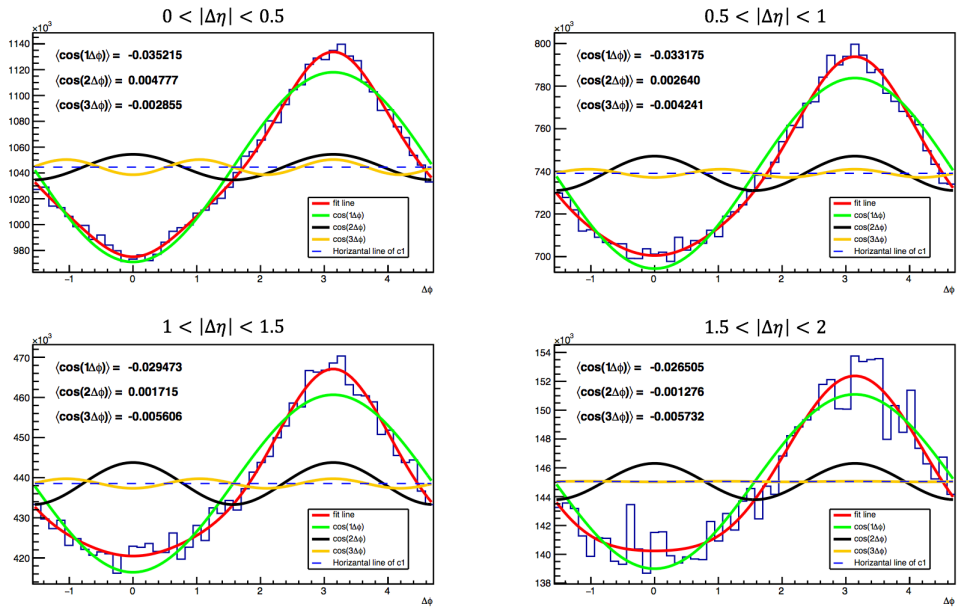


Fig. 4.6 Correlation functions as calculated from 10 million central p+p collisions at 200 GeV, including partonic and hadronic scattering stages. Same labels as the previous plot.

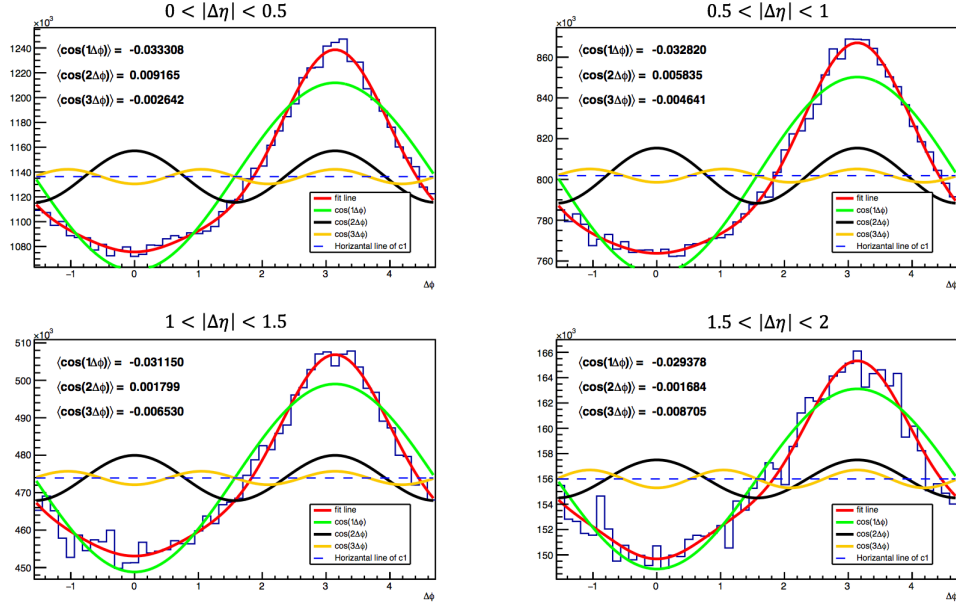


Fig. 4.7 Same correlation functions as in the previous plot, for p+p simulations where partonic and hadronic scattering have not been included. Same labels as the previous plot.

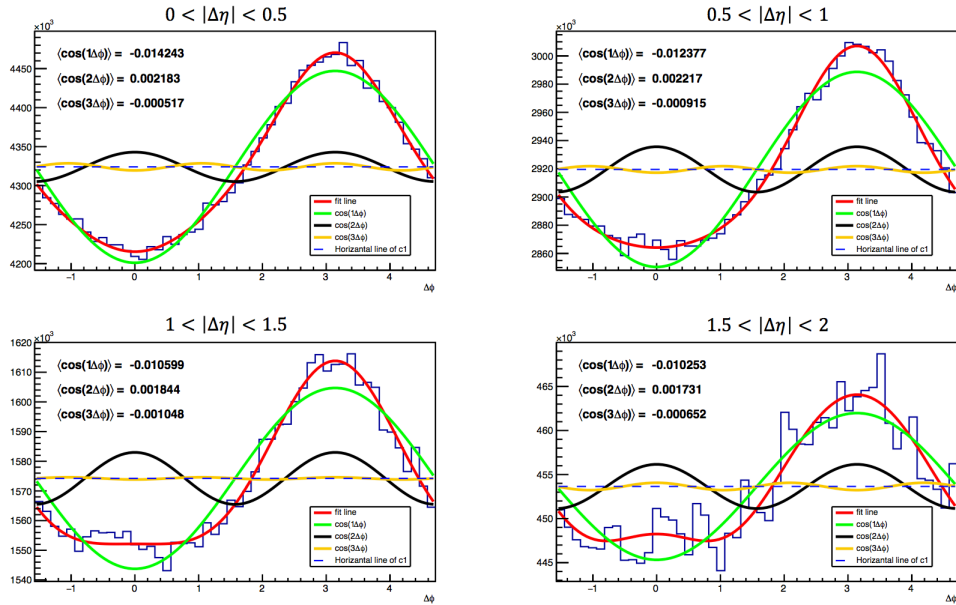


Fig. 4.8 Correlation functions as calculated from 3 million central p+p collisions at 200 GeV, including partonic and hadronic scattering stages. Same labels as the previous plot.

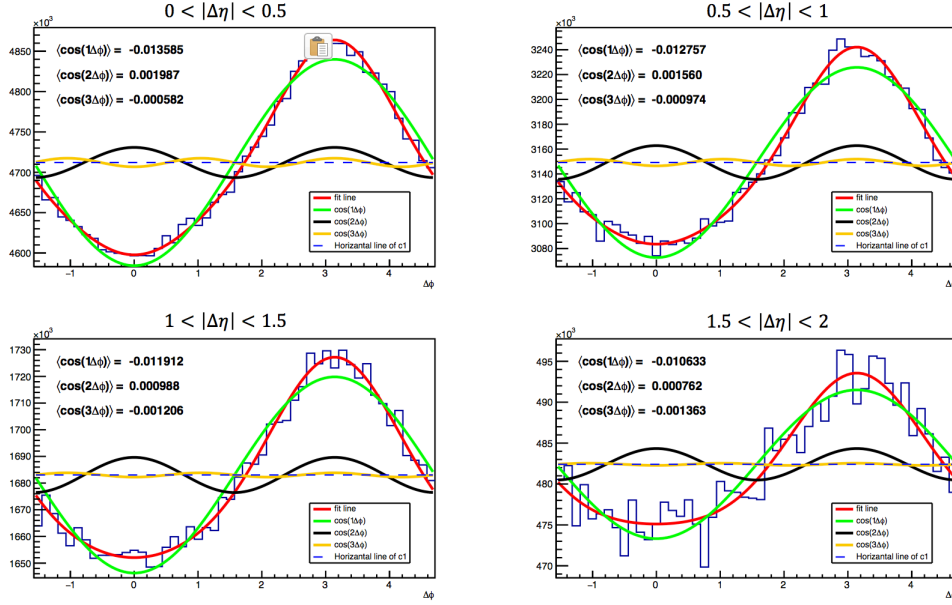


Fig. 4.9 Same correlation functions as in the previous plot, for d+Au simulations at 20 GeV, where partonic and hadronic scattering have not been included. Same labels as the previous plot.

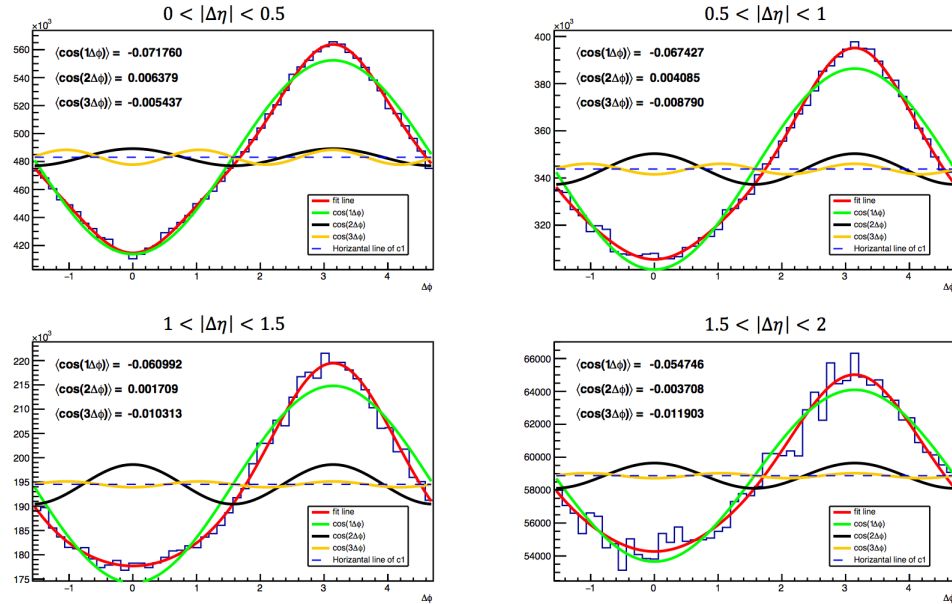


Fig. 4.10 Correlation functions as calculated from 10 million central p+p collisions at 20 GeV, including partonic and hadronic scattering stages. Same labels as the previous plot.

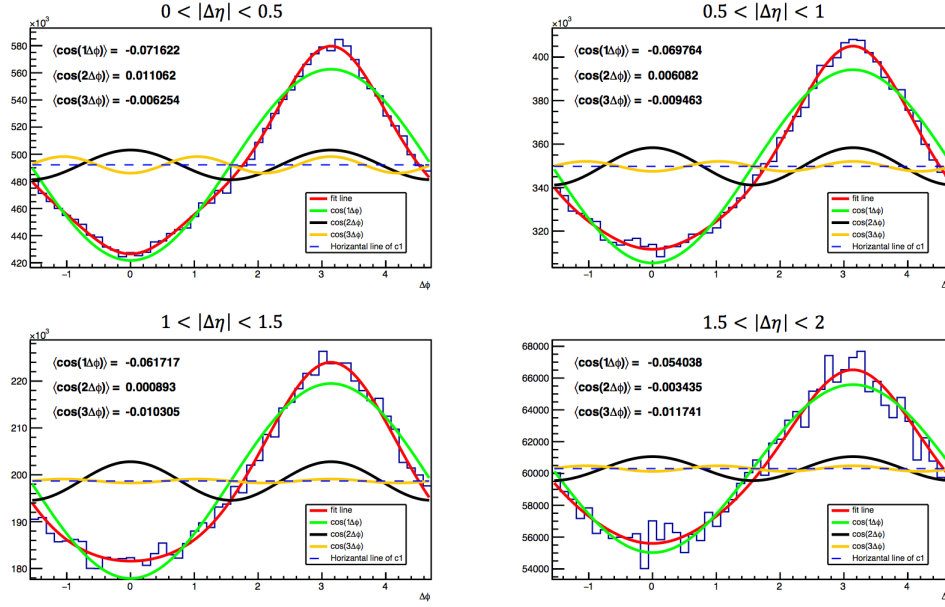


Fig. 4.11 Same correlation functions as in the previous plot, for p+p simulations at 20 GeV, where partonic and hadronic scattering have not been included. Same labels as the previous plot.

### 4.3 Comparing Different Analysis Methods in AMPT Simulations of d+Au Collisions

The participant plane method is only available in simulations and, in theory, it should provide the most accurate and precise estimation of the reaction plane of the collision. We seek to apply this method to compute azimuthal anisotropy coefficients, and to compare it with other methods available for use on real data.

In this study, we calculate the participant plane using initial state nucleons, whose spatial coordinates are smeared by a Gaussian distribution. The participant plane determined in this way is called the “nucleon participant plane”. In addition, we can use the coordinates of partons emitted after string melting to calculate another plane, called the “parton participant plane”. Figure 4.12 shows a comparison of the initial coordinates of partons and nucleons for the same particular d+Au event. In AMPT, every successive interaction of partons and hadrons is

influenced by this initial geometric configuration of partons. Hence, we believe that the parton participant plane calculated with AMPT provides an even more accurate estimation of the initial geometry than the nucleon participant plane (though the final results when using both planes are found to be quite close to each other).

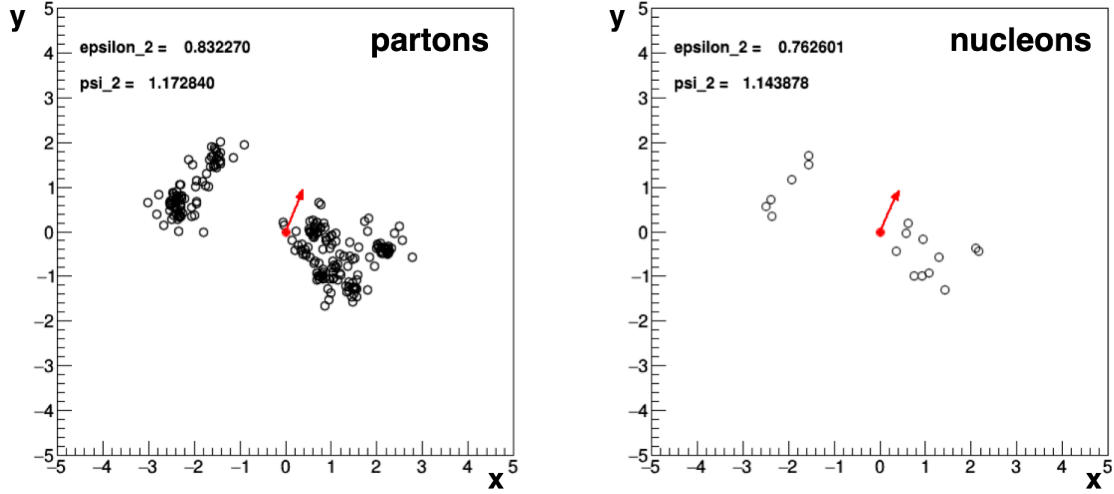


Fig. 4.12 The coordinates of partons (left) and initial state nucleons (right) from the same d+Au AMPT event. The eccentricity and second-order participant plane angle are listed on the upper-left corner. The red arrow indicates the direction of the participant plane.

Firstly, we tested two different methods of computing  $v_2$ : the event plane method and the two-particle cumulant method. Figure 4.13 shows the results of applying these methods to Au+Au events at 200 GeV, with  $b \approx 10 fm$ , which constitutes our large collisions system. As expected, the  $v_2$  curves calculated with the parton and nucleon participant planes are in almost perfect agreement. In addition, the results from all methods agree with each other to within 10% when using the parton participant plane (see ratios on the bottom panel of Figure 4.13). This graph reveals that non-flow effects in large collision systems are quite small, and that the signal is dominated by flow from the initial geometry and subsequent particle interactions.

We then applied the same calculations to the small collision system, d+Au at 200 GeV with  $b < 2 fm$ , using AMPT version 2.26. Results are shown in Figure 4.14. Here, we observe an obvious difference between the result using the participant plane and the other two

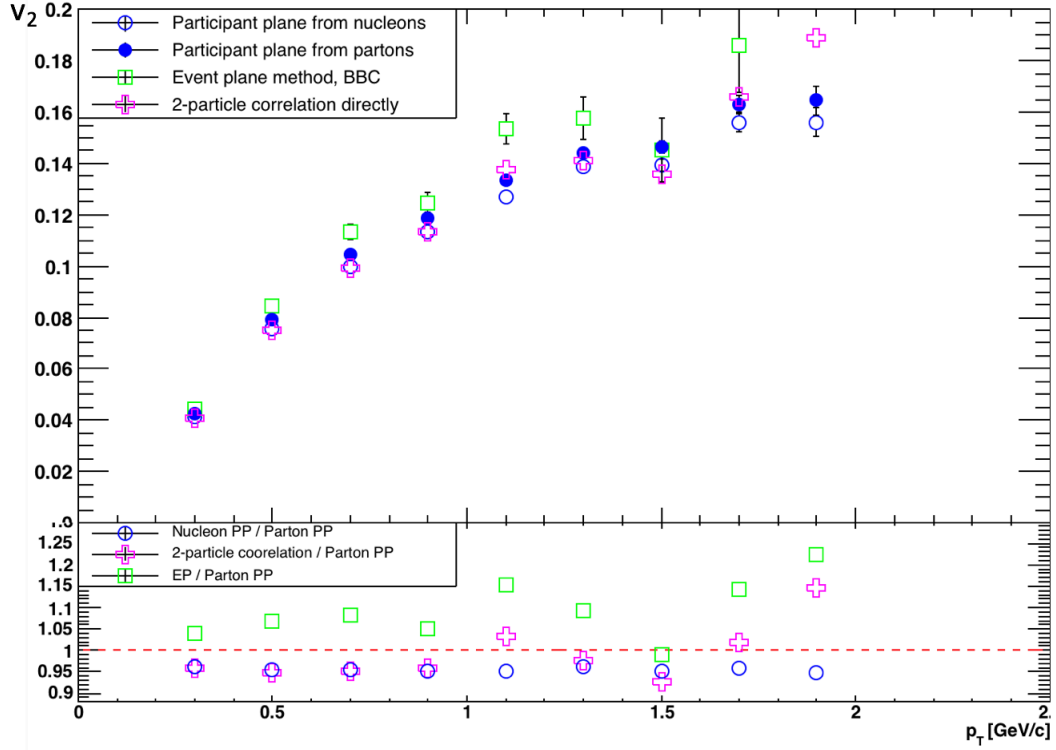


Fig. 4.13 (1) Top:  $v_2(p_T)$  in Au+Au collisions at 200 GeV from AMPT, measured using three different analysis methods: the two-particle cumulant method (pink cross), the event plane method relative to BBC-south region (green box), the parton participant plane method (solid circles), and the nucleon participant plane method (open circles). (2) Bottom: ratio of  $v_2$  from different methods to that from the parton participant plane. Same labels as in the top panel.

methods, which should have contributions from non-flow effects. The lower energy density and multiplicity in small collision systems (compared to large collision systems) does not create as much flow in the QGP. At larger transverse momentum, non-flow effects become larger, and the various results diverge.

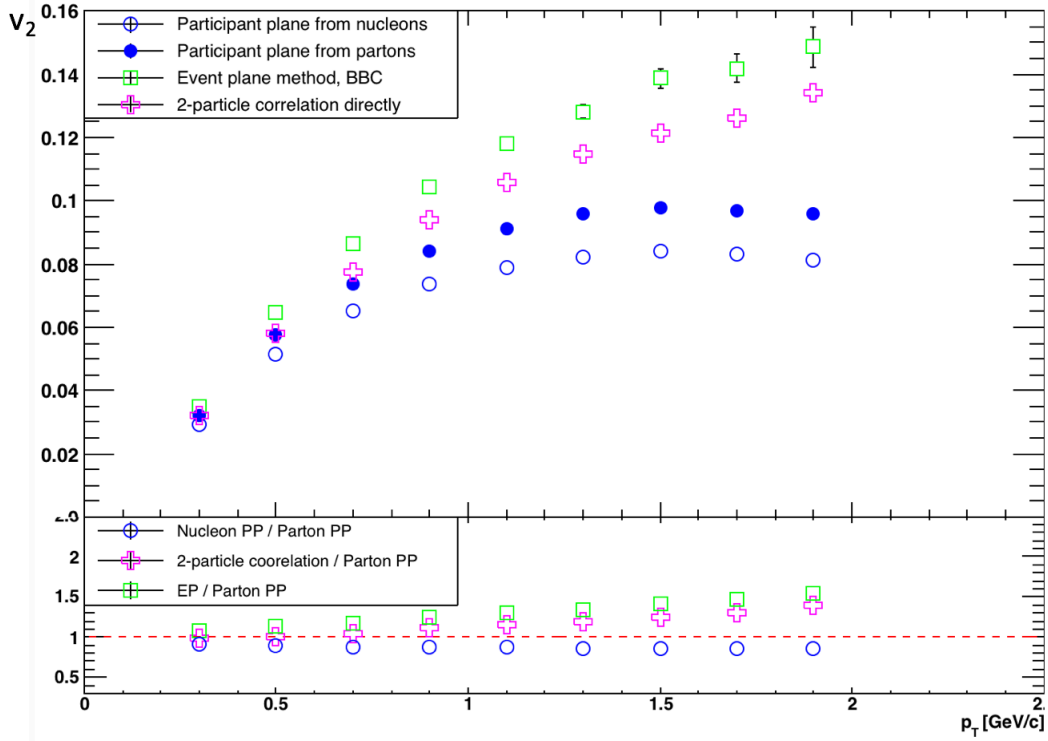


Fig. 4.14 (1) Top:  $v_2(p_T)$  in d+Au collisions at 200 GeV from AMPT, measured using three different analysis methods. Labels are the same as shown in the previous plot. (2) Bottom: ratio of  $v_2$  from different methods to that from the parton participant plane. Same labels as in the top panel.



## 4.4 Reducing Non-flow Effects Through Multi-particle Correlation Methods

Here we present results on the multiplicity dependence of elliptic flow by applying the multi-particle cumulant method and equations 3.19 and 3.20. We used AMPT version 2.26 to simulate minimum bias events for the following collision systems: Pb+Pb at 5.02 TeV, p+Pb at 5.02 TeV, Au+Au at 200 GeV and d+Au at 200 GeV. We applied an acceptance cut, accepting only particles within  $|\eta| < 2.4$  and  $p_T < 3$  GeV/c, which are the same cuts applied by the CMS experiment in their analyses. We also imposed an  $\eta$  gap of  $|\Delta\eta| > 2$  for the two particle cumulant method.

The result for p+Pb is shown in Figure 4.15. We used the parton participant plane method (shown as solid diamonds) as our true plane and compared it with the result from the multi-particle cumulant method. As we expected from Equations 3.10 and 3.11, the result from the two-particle cumulant method is higher than that of the parton participant plane (red open circles), and the result from the four-particle cumulant method is below the parton participant plane. If we compare these results with published results from CMS [6] shown in Figure 4.16, we see that the  $v_2$  as calculated with the 2-particle and 4-particle cumulant methods agrees with the published data.

Figure 4.17 shows results from Pb+Pb collisions at 5.02 TeV. The  $v_2$  averaged from the 2-particle cumulant and the 4-particle cumulant agree perfectly with the  $v_2$  calculated from the parton participant plane. The fluctuation of  $v_2$  and eccentricity are compared in Figure 4.18. From the figure, we can conclude that the fluctuations of  $v_2$  are proportional to the fluctuations of  $\epsilon_2$  in Pb+Pb.

In Au+Au collisions at 200 GeV (Figure 4.19), we also included a calculation with the 2-particle cumulant method without imposing the  $\eta$  gap (red solid circles). It is higher than the curve with the imposed  $\eta$  gap (as expected due to large non-flow effects). As we expected, the

$v_2$  averaged from 2-particle and 4-particle cumulants agrees perfectly with the  $v_2$  calculated with the parton participant plane method.

The most amazing results are from the d+Au system at 200 GeV, as shown in Figure 4.20. The two diamond curves agree perfectly with each other. We therefore infer that it is reasonable to apply this calculation in a real data analysis from PHENIX Run 2016, to get a better estimation of flow.

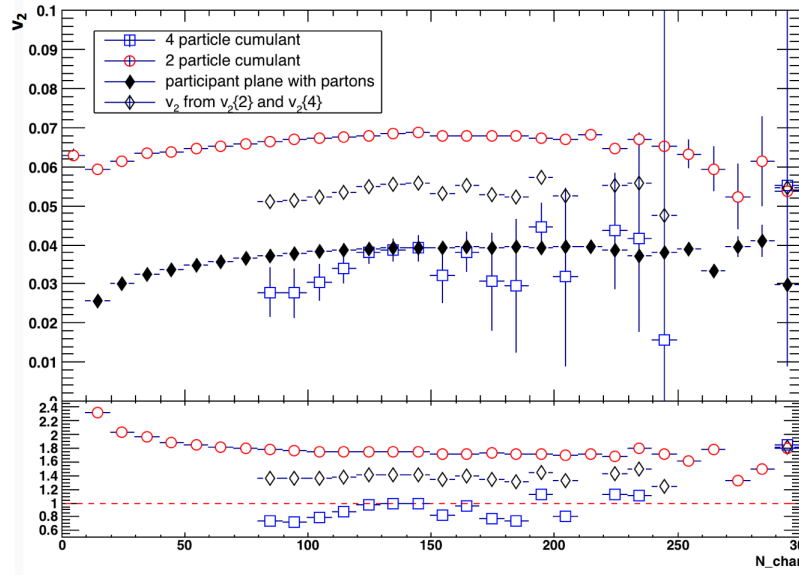


Fig. 4.15 AMPT Simulation of p+Pb collisions at 5.02 TeV. (1) Top:  $v_2$  as a function of the number of charged particles in each event. The red curve is obtained using 2-particle cumulants (with an imposed  $\eta$  gap). The blue curve is from 4-particle cumulants. The solid black diamond curve is the result from the parton participant plane method. Finally, the open black diamond curve shows the results from Equation 3.19. (2) Bottom: ratio of the each set of results to those from the parton participant plane method. Same symbols as in top panel.

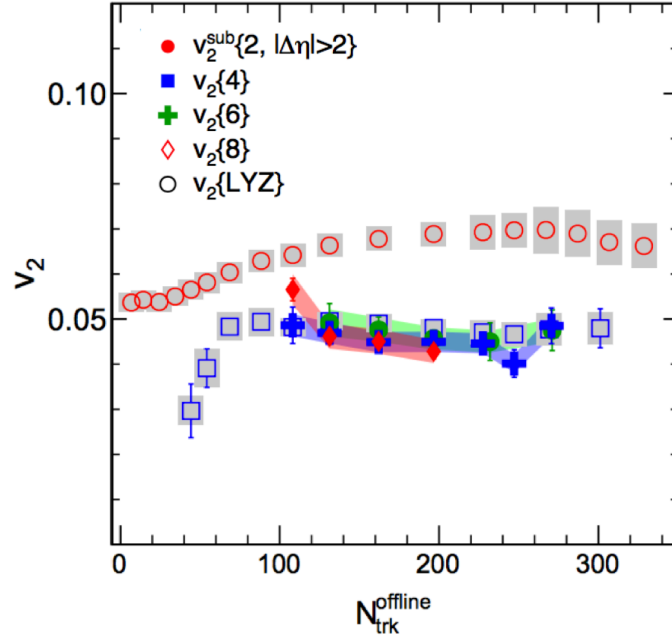


Fig. 4.16 CMS results for  $v_2$  as a function of multiplicity in p+Pb collisions at 5.02 TeV. The red circles are the results from the 2-particle cumulant method. The open blue boxes are from the 4-particle cumulant method. The other symbols are described on the figure [6].

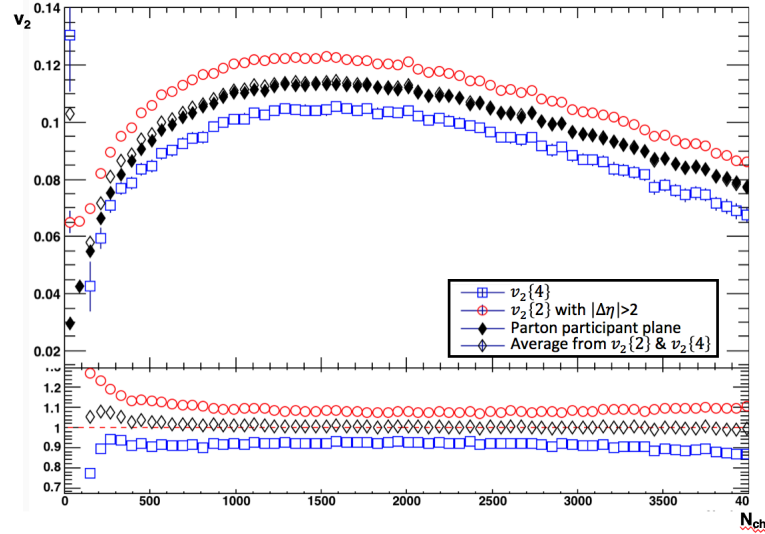


Fig. 4.17 Results from AMPT Pb+Pb events at 5.02 TeV. The labels are the same as in the figure showing the p+Pb results.

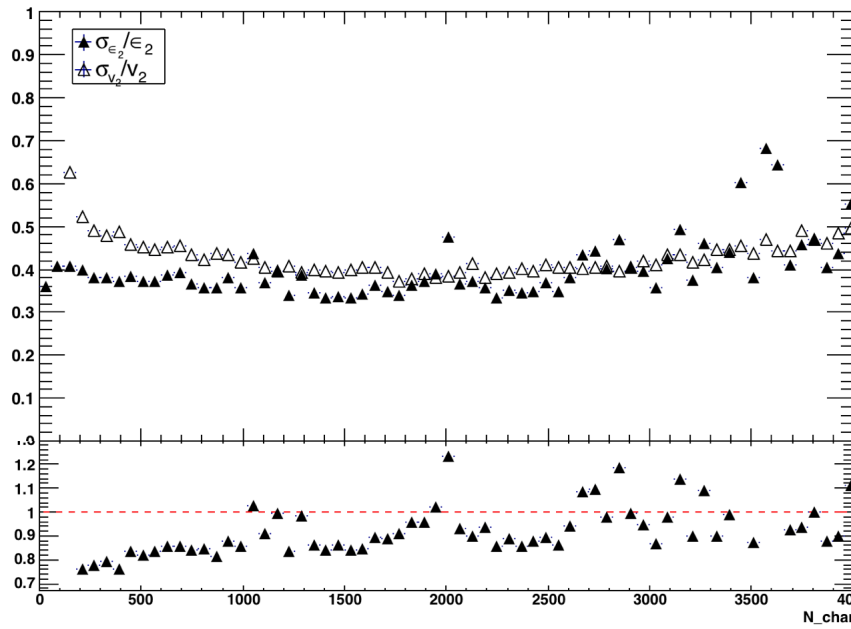


Fig. 4.18 Results from AMPT Pb+Pb events at 5.02 TeV. (1) Top: fluctuations as a function of event multiplicity. The open triangles are the fluctuation of  $v_2$ . The solid triangles are the fluctuation of eccentricity ( $\epsilon_2$ ). (2) Bottom: ratio of the fluctuation of the eccentricity to the fluctuation of  $v_2$ .

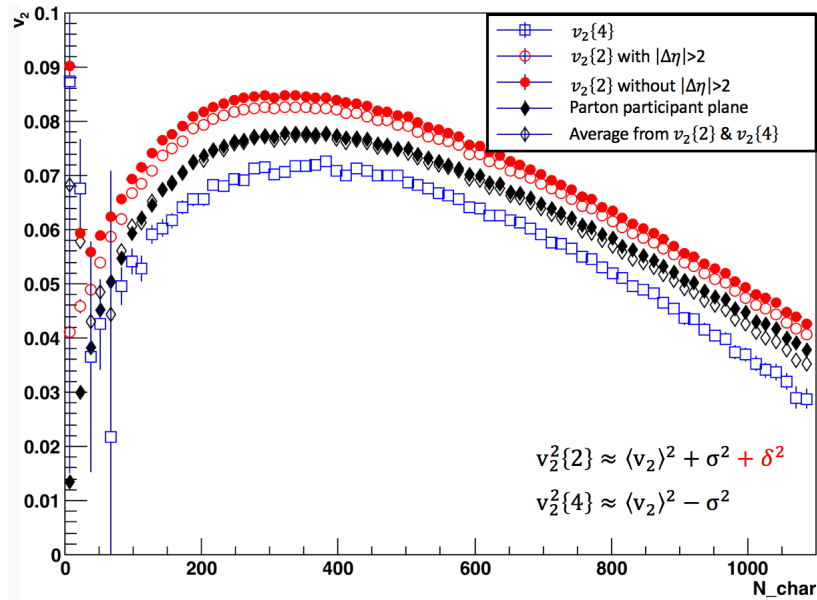


Fig. 4.19 Results from AMPT Au+Au events at 200 GeV. The red solid circle curve shows the result from the 2-particle cumulant method without imposing an  $\eta$  gap. The other labels are the same as above.

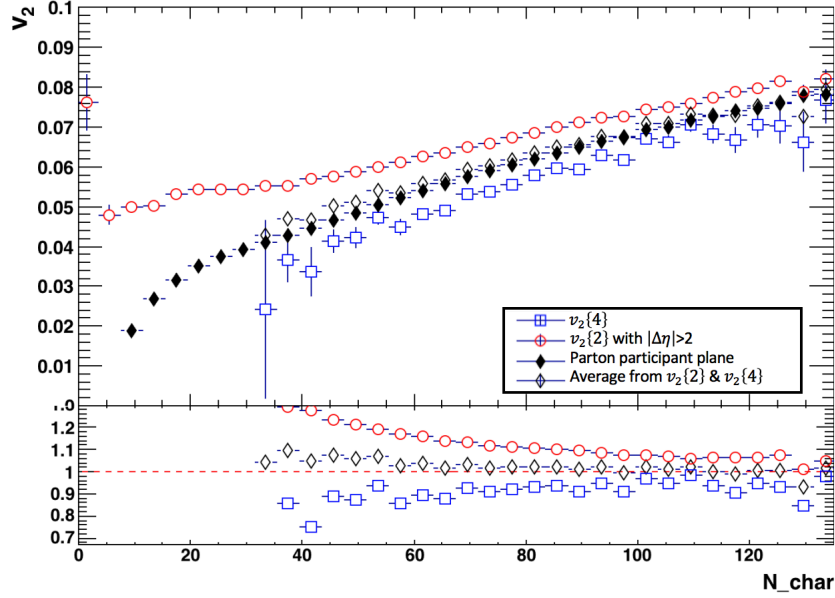


Fig. 4.20 Results from AMPT d+Au events at 200 GeV. The labels are the same as above.

## 4.5 Centrality Dependence of Elliptic Flow in d+Au Collisions

As mentioned before, different collision centralities result in totally different collision geometries and multiplicities. In the most central events, we will generally have a higher energy density and higher number of particles produced than in more peripheral events.

My last topic concerns the centrality dependence of elliptic flow in d+Au at 200 GeV. We divide d+Au events into six different centrality bins based on the number of particles that hit the BBC-south detector region, as shown in Figure 2.2. Then we apply the event plane method and the parton participant plane method to events in each centrality bin. The results are presented in Figure 4.21. As shown in the plots, for central events (0% – 20%), the results from the event plane method (red curves) agree almost perfectly with the parton participant plane method (blue curve), even when the  $p_T$  is around 2.5 GeV. However, as centrality goes down for the peripheral events, the event plane signals increase rapidly, as caused by non-flow effects.

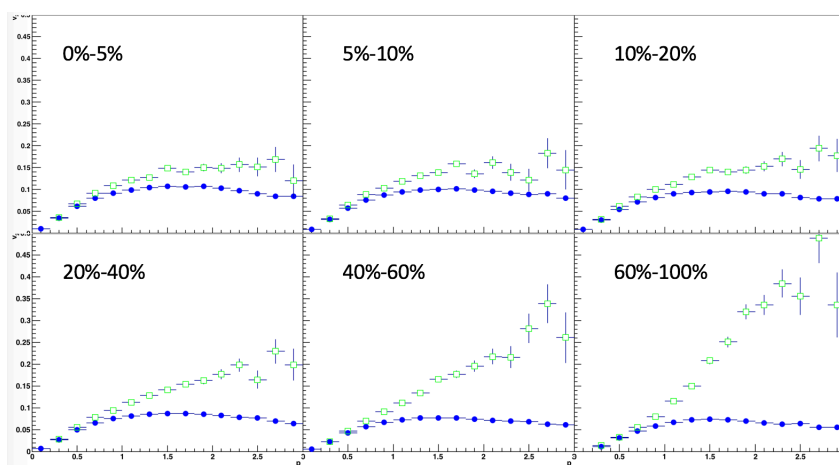


Fig. 4.21 Results from AMPT d+Au events at 200 GeV. Centralities are labeled on each graph. The red curve is  $v_2$  from the event plane method, while the blue curve is  $v_2$  from the parton participant plane method.

# Chapter 5

## Summary

I simulated different collision systems at different energies with the AMPT model and the UrQMD model. The study of  $dN_{ch}/d\eta$  with the UrQMD model helped the PHENIX collaboration develop a set of data acquisition triggers for the beam energy scan. The experiment ran successfully, and my calculations can be compared to actual measurements which will be published soon by PHENIX. The study of  $\eta$  gaps in d+Au and p+p with AMPT demonstrates that a large  $\eta$  gap can reduce the non-flow effects from the collision event signal. I applied the event plane, the participant plane, and multi-particle cumulant methods. The results from multiplicity dependence study, momentum dependence study, and centrality dependence study with these methods give a comprehensive view of the non-flow effects in small collision systems.

At this time, we can not say that we fully understand the non-flow effects. Although we have a good estimate of the flow in small collision systems with AMPT simulations, we still need to compare these results with real data, and the comparison with data analyzed by PHENIX from d+Au collisions at RHIC at 2016 will give a better understanding of non-flow effects in small collision systems.





# References

- [1] Wikipidia. Wikipidia. [https://en.wikipedia.org/wiki/Standard\\_Model](https://en.wikipedia.org/wiki/Standard_Model).
- [2] William A. Zajc Michael Riordan. The First Few Microseconds. *SCIENTIFIC AMERICAN*, pages 34–41, 2006.
- [3] C. Aidala et al. The PHENIX Forward Silicon Vertex Detector. *Nucl. Instrum. Meth.*, A755:44–61, 2014.
- [4] Raimond Snellings. Elliptic Flow: A Brief Review. *New J. Phys.*, 13:055008, 2011.
- [5] Barbara V. Jacak and Berndt Muller. The exploration of hot nuclear matter. *Science*, 337:310–314, 2012.
- [6] Vardan Khachatryan et al. Evidence for Collective Multiparticle Correlations in p-Pb Collisions. *Phys. Rev. Lett.*, 115(1):012301, 2015.
- [7] John W. Harris and Berndt Muller. The Search for the quark - gluon plasma. *Ann. Rev. Nucl. Part. Sci.*, 46:71–107, 1996.
- [8] A. Bazavov et al. Equation of state and QCD transition at finite temperature. *Phys. Rev.*, D80:014504, 2009.
- [9] Paul Romatschke. Light-Heavy Ion Collisions: A window into pre-equilibrium QCD dynamics? *Eur. Phys. J.*, C75(7):305, 2015.
- [10] M. Habich, J. L. Nagle, and P. Romatschke. Particle spectra and HBT radii for simulated central nuclear collisions of C + C, Al + Al, Cu + Cu, Au + Au, and Pb + Pb from  $\sqrt{s} = 62.4 - 2760$  GeV. *Eur. Phys. J.*, C75(1):15, 2015.
- [11] John Novak, Kevin Novak, Scott Pratt, Joshua Vredevogd, Chris Coleman-Smith, and Robert Wolpert. Determining Fundamental Properties of Matter Created in Ultrarelativistic Heavy-Ion Collisions. *Phys. Rev.*, C89(3):034917, 2014.
- [12] J. D. Orjuela Koop, R. Belmont, P. Yin, and J. L. Nagle. Exploring the Beam Energy Dependence of Flow-Like Signatures in Small System  $d$ +Au Collisions. *Phys. Rev.*, C93(4):044910, 2016.
- [13] Zi-Wei Lin, Che Ming Ko, Bao-An Li, Bin Zhang, and Subrata Pal. A Multi-phase transport model for relativistic heavy ion collisions. *Phys. Rev.*, C72:064901, 2005.

- 
- [14] Xin-Nian Wang and Miklos Gyulassy. hijing. *Phys. Rev. D*, 44:3501–3516, Dec 1991.
  - [15] Guo-Liang Ma and Zi-Wei Lin. Predictions for  $\sqrt{s_{NN}} = 5.02$  TeV Pb+Pb Collisions from a Multi-Phase Transport Model. *Phys. Rev.*, C93(5):054911, 2016.
  - [16] Hannah Petersen, Marcus Bleicher, Steffen A. Bass, and Horst Stocker. UrQMD v2.3: Changes and Comparisons. 2008.
  - [17] Michael L. Miller, Klaus Reygers, Stephen J. Sanders, and Peter Steinberg. Glauber modeling in high energy nuclear collisions. *Ann. Rev. Nucl. Part. Sci.*, 57:205–243, 2007.
  - [18] Sergei A. Voloshin, Arthur M. Poskanzer, Aihong Tang, and Gang Wang. Elliptic flow in the Gaussian model of eccentricity fluctuations. *Phys. Lett.*, B659:537–541, 2008.
  - [19] Arthur M. Poskanzer and S. A. Voloshin. Methods for analyzing anisotropic flow in relativistic nuclear collisions. *Phys. Rev.*, C58:1671–1678, 1998.
  - [20] Ante Bilandzic, Raimond Snellings, and Sergei Voloshin. Flow analysis with cumulants: Direct calculations. *Phys. Rev.*, C83:044913, 2011.